Boiling of catechol secondary organic aerosol when heated to mild temperatures (36-52 °C) due to carbon dioxide formation and high viscosity

Kristian J. Kiland,^{1,†} Katherine S. Hopstock,² Ayomide A. Akande,¹ Kristen N. Johnson,² Yixin Li,² Fabian Mahrt,^{1,‡} Sepehr Nikkho,¹ Barbara J. Finlayson-Pitts,² Nadine Borduas-Dedekind,¹ Sergey A. Nizkorodov,² and Allan K. Bertram^{1,*}

- 1 Department of Chemistry, The University of British Columbia, Vancouver V6T 1Z1 British Columbia, Canada
- 2 Department of Chemistry, University of California, Irvine, Irvine, CA 92697, USA.
- † Now at the Department of Integrative Oncology, British Columbia Cancer Research Institute, Vancouver V5Z 1L3, British Columbia, Canada.
- ‡ Now at the Laboratory of Atmospheric Chemistry, Paul Scherrer Institute, Villigen 5232, Switzerland.

Keywords

Catechol, secondary organic aerosol, thermal decomposition, decarboxylation, viscosity

Synopsis

Aerosols' response to heat is needed to accurately interpret thermal desorption measurements. This study reports on a type of aerosol from wildfires which boils when heated to mild temperatures.

Abstract

Thermal desorption measurements, including thermal desorption mass spectrometry, are often used to determine the volatility and chemical composition of secondary organic aerosol (SOA). Accurately interpreting such measurements requires understanding the response of SOA to heat. Using optical microscopy, we monitored catechol + O₃ SOA during heating at mild temperatures (36-52 °C). Catechol + O₃ SOA is a type of SOA formed in wildfire plumes. Surprisingly, the SOA particles appeared to boil when heated to these temperatures. We identified acetone and CO₂ as dominant species emitted from the SOA during heating, implying decomposition of the SOA components. Using mass spectrometry techniques, we observed catechol dimers to be the major product in unheated SOA and observed the degradation of these dimers after heating. Viscosity calculations suggested the mixing time of acetone and CO₂ within the particles was 11 h and 1 h at temperatures of 36 and 52 °C, respectively. The observed boiling can be explained by the production and slow mixing of CO₂ within the SOA particles when subjected to mild temperatures. Our results underscore the importance of considering decomposition, high viscosities, and slow mixing times when interpreting thermal desorption measurements of SOA, even when heating to mild temperatures.

1. Introduction

Biomass burning, including wildfires, emits large amounts of volatile organic compounds (VOCs) into the atmosphere. One major class of VOCs emitted from biomass burning is phenolic compounds. Once in the atmosphere, phenolic compounds will be oxidized by OH, O3, and NO3 to form lower volatility products, which can form new secondary organic aerosol (SOA) particles or partition to the particle phase to grow pre-existing SOA. And SOA can contribute to poor air quality and can influence climate by directly scattering or absorbing solar radiation or by acting as nuclei for clouds. And solve the solution of the particle phase to grow pre-existing or absorbing solar radiation or by acting as nuclei for clouds.

To predict the environmental impacts of SOA, information on their volatility and chemical composition is needed. Thermal desorption (TD) techniques are widely used to determine both of these properties. TD techniques coupled with particle sizing instruments are often used to determine the volatility of SOA, and TD techniques coupled with mass spectrometers are often used to determine both volatility and chemical composition. To interpret TD measurements, information on the thermal stability (i.e., resistance to thermal decomposition) of SOA components is needed. Several previous studies have investigated the thermal stability of SOA components and showed that some SOA components can decompose when heated to temperatures used in TD experiments. However, no studies have investigated the thermal stability of catechol + O₃ SOA. Catechol (Fig. S1) is a phenolic VOC emitted during biomass burning, and it produces SOA upon oxidation by O₃. Although not studied here, catechol + OH and catechol + NO₃ can also produce SOA.

To interpret results from TD measurements, information is also needed on the viscosity of SOA when heated. When converting TD measurements to volatilities, researchers have often assumed that the SOA particles are well mixed, i.e., that the organic molecules are homogeneously mixed throughout the SOA particle. This assumption implies that the SOA viscosity is low and viscosity is not a kinetic barrier to evaporation. Alternatively, researchers have assumed that viscosity can provide a kinetic barrier to evaporation, but this kinetic barrier does not change with temperature and can be described using an effective mass accommodation coefficient. Information on the viscosities of SOA at temperatures commonly used in TD measurements is needed to test these assumptions. Also related to the previous paragraph, thermal decomposition of SOA components when heated could lead to a change in SOA viscosity, since composition and viscosity are tightly connected. Many studies have investigated the viscosities of SOA at room temperature, the studies attention has focused on the viscosity of SOA upon heating, that focus on viscosity of SOA upon heating, researchers often assume that thermal decomposition of SOA components does not occur when aerosols are heated to mild temperatures.

Recently, we developed a hot-stage microscopy technique for measuring the temperature-dependent viscosity of SOA. ⁴² This technique involves heating an SOA sample with non-spherical geometries and quantifying the change in shape of the SOA sample due to heating with an optical microscope. From the shape change, viscosities can be calculated. This method worked as expected for farnesene SOA. ⁴² However, when attempting to measure the temperature-dependent viscosity of SOA generated by the ozonolysis of catechol, surprisingly, the volume of the SOA increased when heated to mild temperatures (36-52 °C).

The chemical composition of SOA formed by the ozonolysis of catechol has only been investigated in a few studies. Pillar-Little et al. experimentally investigated the heterogeneous oxidation of catechol thin films by ozone, observing the formation of muconic acid. Further oxidation of muconic acid resulted in a range of acids, including glyoxylic, oxalic, crotonic, maleic, glutaconic, 4-hydroxy-2-butenoic, and 5-oxo-2-pentenoic acids. Additionally, indirect oxidation by in situ produced OH led to the generation of semiquinone radical intermediates, contributing to the synthesis of polyhydroxylated aromatic rings such as tri-, tetra-, and penta-hydroxybenzene. Sun et al. conducted theoretical investigations on the oxidation of catechol by ozone, predicting 2-hydroxy-6-oxohexa-2,4-dienoic acid, 5-(carboxyoxy)-2reaction products such as hydroxypenta-2,4-dienoic acid, 1-hydroxy-5-oxopenta-1,3-dien-1-yl hydrogen carbonate, oxalaldehyde, malealdehyde, and oxalic acid. 45 Barnum et al. investigated the ozonolysis of catechol in both condensed and gas phases using experimental and theoretical approaches. They identified muconic acid as the dominant reaction product.⁴⁶

Here, we focus on the unique physical and chemical properties of catechol + O₃ SOA when heated to mild temperatures (36-52 °C). We used an optical microscope to monitor the change in size and morphology during heating of the SOA to mild temperatures (36-52 °C). To better understand the optical microscope results and the thermal stability of the components, we used three different mass spectrometry techniques to measure the composition of the gas and particle phase before, during, and after heating. We also calculated the viscosity of the SOA at temperatures up to 52 °C. The implications of these results for interpreting TD measurements are discussed.

2. Materials & methods

2.1. SOA generation

SOA was generated from the dark ozonolysis of catechol in a continuous-flow environmental chamber, described in detail elsewhere. In addition, α -pinene + O₃ SOA was generated by the dark ozonolysis of α -pinene in the same environmental chamber and used as a reference system for some of the experiments. For the remainder of the document, we refer to catechol + O₃ SOA and α -pinene + O₃ SOA as just catechol SOA and α -pinene SOA, respectively.

The environmental chamber was a 1.8 m³ Teflon bag housed within an aluminum enclosure. The flow rate through the chamber was ~18 L min⁻¹, resulting in a mean residence time in the chamber of ~1.7 h. Both the VOCs and O₃ were carried into the chamber via pure air streams. For the VOC feed line, a 2 wt% solution of catechol or α-pinene in 2-butanol was injected into a heated round bottom flask using a syringe pump. The injection rate for both catechol and α-pinene was 30 μL h⁻¹. 2-butanol was used as a scavenger for OH radicals which can be generated as a by-product of ozonolysis reactions. Cavalli et al. showed that the major oxidation products of butanol + OH are butanal, propanal, ethanal, and formaldehyde. The vapor pressures of these molecules are high, likely preventing a large amount of the products from partitioning into the particle phase. Furthermore, butanol has been used as an OH scavenger in a large number of chamber experiments because its oxidation products do not contribute significantly to SOA mass. For the O₃ feed line, pure air flowed through an ozone generator (UV-pen lamp; Jelight, model 610) and into the chamber. Both the ozone concentration and aerosol mass loading were measured at the outlet of the chamber. Ozone was in excess and was measured to be ~325–370 ppb using an O₃ monitor

(49i, Thermo Scientific). The mass loading in the chamber for catechol SOA ranged from 13–70 μ g m⁻³ during collection. For α-pinene SOA, the mass loading was ~30–55 μ g m⁻³, as measured using an optical particle counter (GRIMM, 11-S OPC). The OPC measures particle sizes from 250 nm to 32 μm. Significant mass was measured for both catechol and α-pinene SOA for diameters between 250 nm to 700 nm, with the most mass measured between 350-450 nm. The resulting SOA particles were collected on hydrophobic glass slides or silicon wafers at the outlet of the chamber using a multi-orifice single-stage impactor with a 50% cut-off diameter of ~0.18 µm (MOSSI, MSP Corporation), operated at a flow rate of 12 L min⁻¹. For imaging experiments, proton-transfer-reaction time-of-flight mass spectrometry (PTR-ToF-MS) analysis, and ultra-highperformance liquid chromatography heated electrospray ionization high-resolution mass spectrometry (UHPLC-HESI-HRMS) analysis, the particles were collected on hydrophobic glass slides (22 mm, Hampton Research Corp., HR3-215). For electron impact mass spectrometry (EI-MS) analysis, the particles were collected on silicon wafers with a native oxide layer (p-type, 111, Wacker Siltronic Inc., Germany). SOA collection times were ~16–27 h. During the collection period, some further oxidation of the SOA may have occurred in the impactor, as O₃ was only removed from the gas stream following the impactor. However, since O₃ was in excess, most of the oxidation likely occurred in the chamber.

2.2. Optical microscopy of SOA material during heating

A temperature-controlled cell (HC321Gi, INSTEC) mounted above a microscope (Axio Observer, Zeiss) was used for imaging the SOA material during heating. The temperature of the cell was controlled by offsetting hot (electrical) and cold (liquid nitrogen) inputs around the inner walls of the cell. We performed some heating experiments while viewing the particles from the top, and others while viewing the particles from the side (Fig. S2). These two orientations required different sample preparation. For the top view experiments, particles on the glass slide were scraped into a pile using a razor blade, and the glass slide was then directly inserted into the temperature-controlled cell. For a side view, the particles on the glass slides were scraped into a pile and then attached to the flat end of an ultra-fine needle (Roboz Surgical Instruments Co.) by bringing the needle surface into contact with the scraped particles. The needle was then inserted into the temperature-controlled cell as detailed previously.⁴² The results and conclusions presented herein were not sensitive to the viewing method (top view vs. side view).

Prior to the imaging experiments, the temperature-controlled cell was purged with nitrogen for a minimum of 15 min and then sealed from the surrounding atmosphere. We also performed additional experiments with the particles exposed to ambient air during heating and found that the results were not sensitive to the type of atmosphere. Imaging experiments were carried out using a temperature ramp rate of 2 °C min⁻¹. Alternatively, the temperature was quickly increased (2 °C s⁻¹) to a set temperature and then held at the set temperature for a certain period of time. Temperatures reported hereafter have been calibrated using melting points of standard materials, described in detail in previous publications. ^{42,49}

2.3. Vocus PTR-ToF-MS characterization of gas-phase vapors during heating

To detect the gas phase molecules emitted by the SOA material while heating, we connected a Vocus PTR-ToF-MS (Tofwerk/Aerodyne) to the temperature-controlled cell

discussed above using a 1/4" OD fluorinated ethylene-propylene (FEP) sample line. A stream of nitrogen air (1000 sccm) continuously flowed through the temperature-controlled cell and into the Vocus to detect gas-phase molecules. Prior to each experiment, the temperature-controlled cell was thoroughly cleaned with isopropyl alcohol and dried with clean air.

After cleaning the cell, the temperature of the cell (without a glass slide) was rapidly heated to 36 °C or 52 °C, and the vapors coming from the cell were monitored for approximately 30 min to determine the background signal from the cell. After the background signal was recorded, a glass slide containing the SOA was introduced into the cell already at 36 °C or 52 °C. The vapors coming from the cell and glass slide (held at 36 °C or 52 °C) were then monitored for 2 h. For each temperature, experiments were performed in triplicate.

A detailed explanation of the Vocus has been published previously. ⁵⁰ Briefly, ionization occurs via chemical ionization using hydronium ions (H_3O^+) as the reagent ion, which is generated by a low-pressure discharge method. The instrument drift tube was operated at a pressure of 2.1 mbar, reactor temperature of 60 °C, single ion signal of 2.75 mVns, and a reduced field strength (E/N) of 130 Td. The ion source was set at 427 V and 2 mA, and the water for the reagent ion flowed constantly at 20 sccm. We collected data at a 1-second time resolution with an inlet flow of ~50 sccm. Mass spectra were recorded from 0-497 m/z, and the Big Segmented Quadrupole (BSQ) of the Vocus was set at 320 V, filtering signals below m/z 45.

Data analysis was done using the Tofware/Igor Pro Package (Aerodyne Inc, Wavemetrics). Peaks were assigned to corresponding molecular weights using a mass accuracy of < 5 ppm deviation from the exact masses.

2.4. EI-MS characterization of gas-phase vapors during heating

To detect vapors coming off the SOA during heating we also used a newly constructed Knudsen cell-temperature programmed desorption apparatus coupled to an electron impact-mass spectrometer (EI-MS). Unlike the Vocus system described above, this system is sensitive to CO and CO₂ vapors in addition to organic gaseous compounds.

For the EI-MS experiments, SOA was impacted onto silicon wafers. The mass on each wafer ranged from 0.28 to 0.45 mg for catechol SOA and 0.47 to 0.65 mg for α -pinene SOA. For each experiment, a wafer was inserted in the vacuum chamber at 25 °C, which was then cooled to -45 °C while purging the chamber with helium gas. After reaching -45 °C, the chamber was pumped down to 1×10^{-4} Torr.

Two types of experiments were conducted. The first involved heating the sample to 75 °C while keeping the sample isolated from the main vacuum chamber. When the sample temperature reached 75 °C, the sample compartment was opened to the main vacuum chamber, releasing a burst of evolved products into the chamber. A full mass spectrum was collected in the mass range of $12-250 \, m/z$ using a quadrupole mass spectrometer (Extrel) with electron impact ionization. The second type of experiment involved linearly heating the sample from -45 °C to 95 °C at a rate of 0.1 °C s⁻¹ while the sample was exposed to the vacuum chamber. During heating, the mass spectrometer was set for single ion monitoring at m/z 44, identified during the first experimental approach. The temperature is held at 95 °C for about 10 min and then allowed to cool to room temperature.

2.5. UHPLC-HESI- HRMS of condensed phase components before and after heating

For analysis of the condensed SOA phase, both unheated and heated catechol SOA samples were used: samples were heated to either 36 °C or 52 °C for 2 h using the temperature-controlled cell used in the optical microscope and the Vocus experiments discussed above. During heating, a stream of nitrogen air (~1 L min⁻¹) continuously flowed through the temperature-controlled cell.

A slide containing catechol SOA (before or after heating) was placed in a beaker and rinsed with 3 mL of acetonitrile and 3 mL of nanopure water. Based on a visual inspection, SOA fully dissolved off the slides shortly upon exposure to solvent. The dissolved SOA was then rotary evaporated and redissolved in 0.5 mL acetonitrile and 0.5 mL nanopure water, as 1:1 (v/v) ACN/H₂O is the solvent system used for HRMS. Blanks of each clean beaker were run on HRMS and factored into the background signal.

Mass spectra were recorded with a Thermo Scientific Vanquish Horizon ultrahigh pressure liquid chromatograph coupled to an electrospray ionization Q Exactive Plus high-resolution mass spectrometer (UHPLC-HRMS) with a resolving power of up to 1.4 x 10⁵ (at *m/z* 200). The separation was performed on a reverse phase column (Phenomenex Luna Omega Polar C18, 150 x 2.1 mm, 1.6 μm particles, 100 Å pores) with the column temperature kept at 30 °C. The eluent flow was 0.3 μL min⁻¹ and consisted of LC-MS grade H₂O acidified with 0.1 % formic acid (solution A) and LC-MS grade acetonitrile with 0.1 % formic acid (solution B). The gradient was: 0-3 min: 95 % A; 3-14 min linear ramp to 95 % B; 14-16 min hold at 95 % B; 16 min return to 95 % A; and 22 min hold in preparation for the next run. Mass spectra were obtained with the *m/z* range of 100-750 in the negative ion mode. The parameters of the heated electrospray ionization (HESI) ion source settings of the Orbitrap were: 2.5 kV spray voltage, 300 °C probe heater temperature, 320 °C capillary temperature, S-Lens ion funnel RF level 30, 50 units of sheath gas (nitrogen) flow, 10 units of auxiliary gas (nitrogen) flow, and 1 unit of spare gas (nitrogen) flow. All SOA samples were run in triplicate.

Chromatograms were analyzed using the Thermo Scientific program FreeStyle 1.6. Integration with the mass spectra was performed between the column's dead time (2 min) and the start of the column re-equilibration time (16 min). Decon2LS program (https://pnnl-comp-mass-spec.github.io) was used to cluster all mass spectra from each temperature (room temperature, heated to 36 °C, and heated to 52 °C). Background peaks only present in the blank samples were removed from all SOA spectra. Peaks containing 13 C isotopes were removed. Mass accuracy of \pm 0.0005 m/z units was used to assign peaks with formulae $C_xH_yO_z$ with restrictions implemented for atomic ratios: C < 40, H < 80, and O < 35. The assigned formulas were corrected for deprotonation in the negative ionization mode and reported as neutral formulae of catechol SOA. Neutral molecular weights were calculated from neutral formulas (approximately equal to the ion's molecular weight plus one).

3. Results and Discussion

3.1. Optical microscopy of SOA material during heating

Optical images of catechol SOA material suspended on a tungsten needle (side view) were recorded while the temperature was increased at 2 °C min⁻¹ (Fig. 1 and Video S1). At approximately 40 °C, the cross-sectional area of the material began to increase. At a temperature

of 80 °C, the cross-sectional area had increased by a factor of ~4 (Fig. 1). Above 80 °C, the cross-sectional area suddenly decreased and then increased several times thereafter. The particles also became less opaque when the cross-sectional area increased. We attribute this cycle of increasing and decreasing cross-sectional area to the boiling of SOA material, with the gradual size increase being due to trapped bubbles growing inside the particle, and the sudden decrease in size being caused by bubbles escaping from the particle.

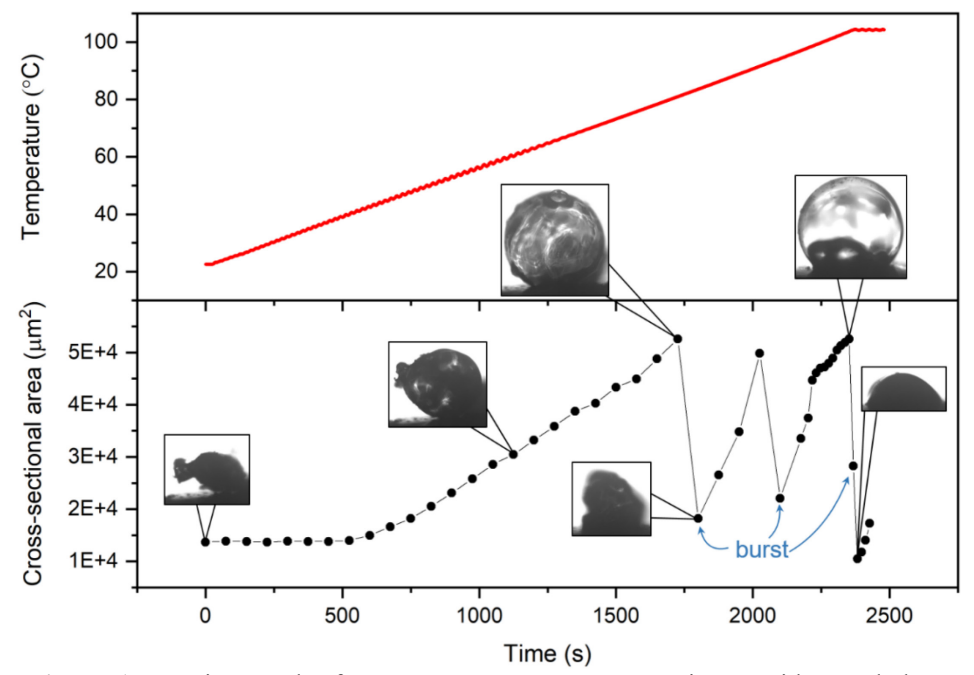


Figure 1. Imaging results from a temperature ramp experiment with catechol SOA. The top panel shows the temperature profile (ramp rate of 2 °C min⁻¹), and the bottom panel shows the corresponding cross-sectional area of the particle. The particle was attached to a needle to capture side-view images. The initial area-equivalent diameter of the particle (at t = 0) was 132 μ m, which grew to a maximum of 259 μ m at 1725 s.

For catechol SOA, the onset of boiling was approximately 40 °C. Side-view heating experiments where the temperature was first increased rapidly and then held at 36 °C were also performed for catechol SOA (Fig. 2 and Video S2). The cross-sectional areas of the SOA particles also increased in these experiments, consistent with the boiling behavior in Fig. 1. Fig. 2 and Video S2 suggest boiling of the catechol SOA occurred even at the mild temperature of 36 °C.

Fig. 3 and Video S3 show SOA material on a hydrophobic glass slide (top view) during rapid heating to 52 °C followed by a constant temperature of 52 °C for approximately 19 min. At 52 °C, the cross-sectional area of the catechol SOA increased, consistent with Fig. 1–2. Additionally, in all our experiments, bubble-shaped inclusions were clearly visible in the SOA, consistent with the boiling of SOA material. In contrast, when α -pinene SOA was heated to 52°C, inclusions were not observed and the cross-sectional area did not increase (Fig. S3).

The absolute increases in cross-sectional area in Fig. 2–3 is dependent on the experimental set-up (i.e., side view *vs.* top view and attached to a needle vs on a hydrophobic glass substrate). Nevertheless, the different geometries and substrates all show boiling behavior when heated to mild temperatures.

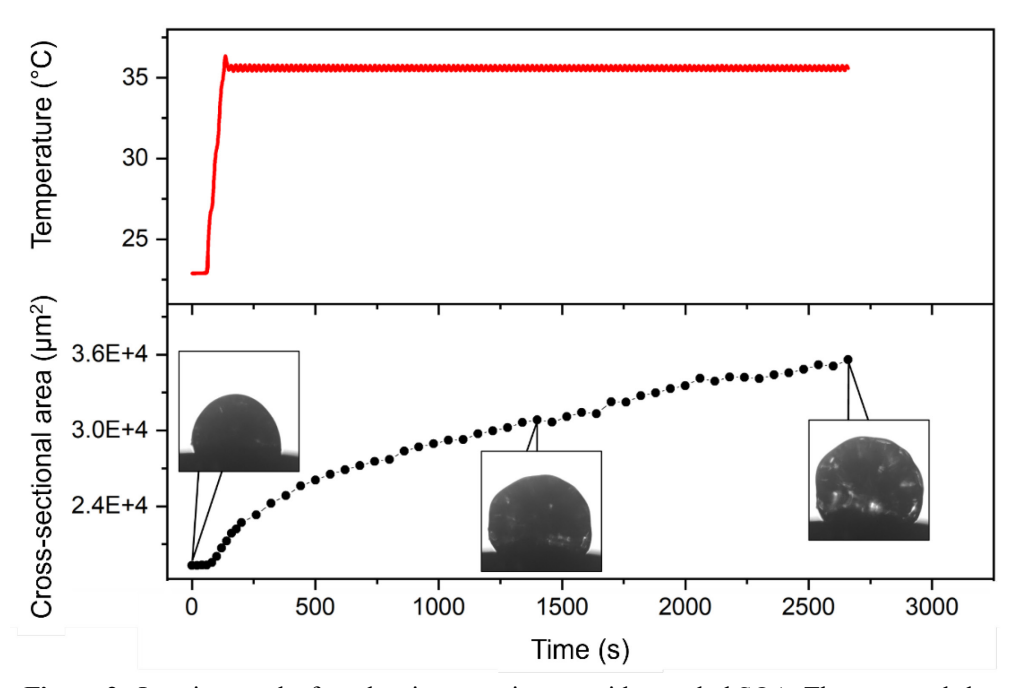


Figure 2. Imaging results from heating experiments with catechol SOA. The top panel shows the temperature profile during heating (T = 36 °C). Corresponding cross-sectional areas of the catechol SOA particle (bottom panel) are shown. The particle was attached to a needle to capture side-view images. All images have dimensions of \sim 265 \times 265 μm .

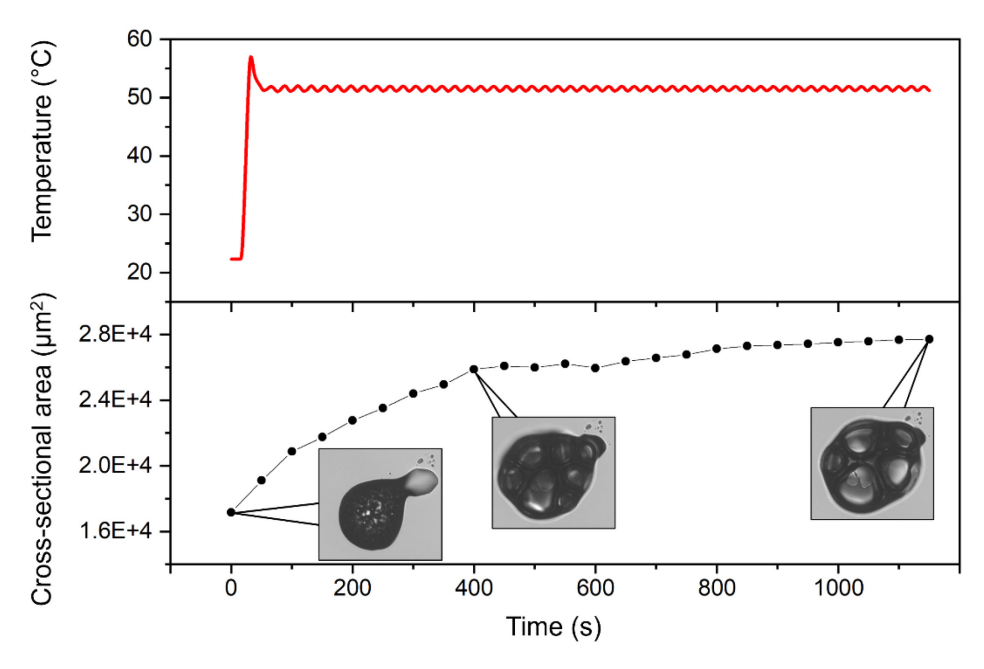


Figure 3. Results from 52 °C heating experiments with catechol SOA. The top panel shows the temperature profile during heating. Corresponding cross-sectional areas of the catechol SOA particle (bottom panel) are shown. Top-view images of the particles on hydrophobic glass slides are provided alongside the data. During heating, bubbles began forming within the catechol SOA particle. All images have dimensions of \sim 240 × 220 μ m.

3.2. Vocus PTR-ToF-MS characterization of gas-phase vapors during heating

To understand which molecules were participating in the boiling behavior of catechol SOA, we built a setup to flow the evolving gas phase molecules into a Vocus. We measured the background vapors from the experimental setup by heating a flow cell to 36 or 52 °C (Fig. S4 and S5). Next, we added the SOA sample to the heated flow cell and observed the vapors that evolved from the heated SOA sample and flow cell combined (Fig. S4 and S5). Difference mass spectra between the sample and heated flow cell show the enhancement of m/z C₃H₇O⁺ and C₃H₉O₂⁺ assigned to acetone and an acetone-water cluster, respectively (Fig. 4). There was a strong correlation between the signals of C₃H₇O⁺ and C₃H₉O₂⁺ (R² = 0.99, Fig. S6). These results indicated that acetone was a dominant species that evolved from the SOA material when heated to 36 or 52 °C.

Traces of the total ion count for the acetone peak and the acetone-water cluster peak as a function of time display the enhancement in acetone during heating of the SOA (Fig. 5). As soon as the catechol SOA sample was introduced to the heated cell (at 1800 s), the total ion signal and the acetone signals rapidly increased followed by a slow decay. The decay of the total ion signal and the acetone signals is likely due to the decay of acetone available to evaporate. Nevertheless, even at a time of 3000 s the total ion signal and the acetone signals were still above background levels recorded prior to introducing the catechol SOA sample into the heated cell.

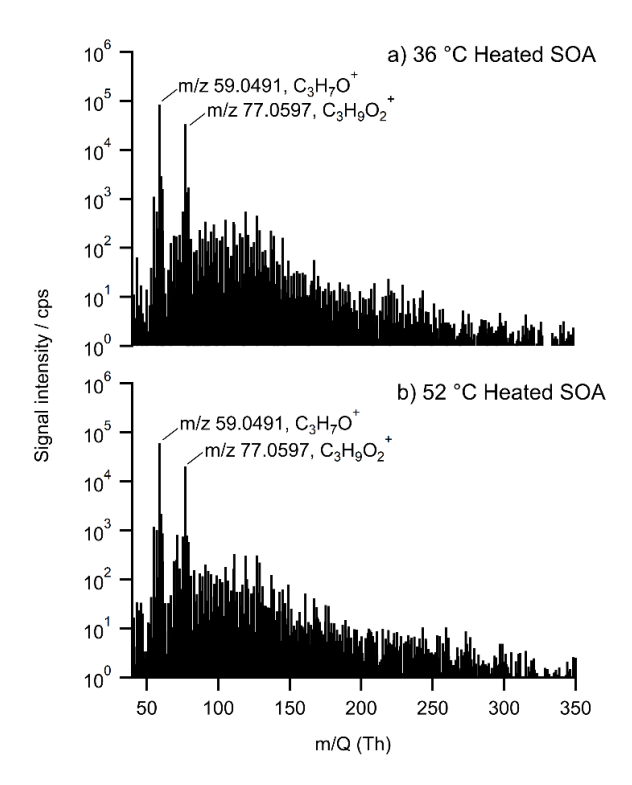


Figure 4. Difference mass spectra measured by the Vocus of the vapors from the flow cell and the vapors from the flow cell and the SOA sample. The total ion counts per second (cps) are plotted as a function of mass to charge ratio during heating (a) to 36 °C, and (b) to 52 °C. Mass spectra of the flow cell background and the flow cell with the sample in it are provided in Section S3.

The high background of acetone observed here (e.g. Fig. 5) is a combination of acetone internally present in the Vocus, which is elevated when the inlet PEEK capillary is obstructed, as shown previously,⁵¹ and acetone outgassing from the empty temperature-controlled flow cell used in the heating experiments. The sum of the internal acetone signal and outgassing from the empty flow cell was slightly enhanced at higher temperatures.

Acetone has been observed previously from the photodegradation of various types of SOA using near-UV radiation (300 nm).^{52,53} Acetone has also been observed as a minor product from the pyrolysis of carboxylic acids, alcohols, and peroxides, although typical at higher temperatures than used in our experiments.⁵⁴ Additional studies are needed to determine the mechanism of acetone production from catechol SOA.

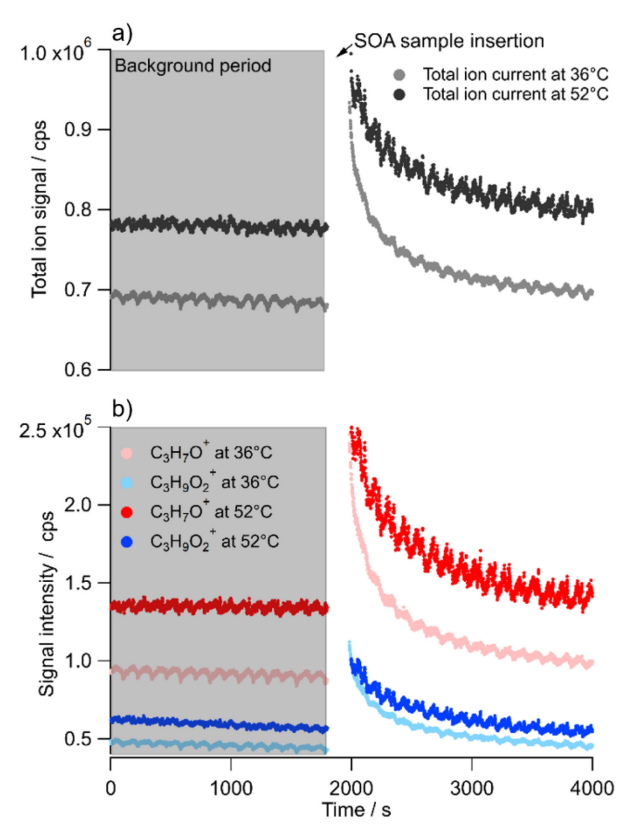


Figure 5. Time dependence traces at 36 °C and 52 °C for (a) the total ion signal and for (b) $C_3H_7O^+$ in red (likely acetone) and $C_3H_9O_2^+$ in blue (likely acetone-water cluster).

3.3. EI-MS characterization of gas-phase vapors during heating

The first type of EI-MS experiment involved heating the sample to 75 °C while keeping the sample isolated from the main vacuum chamber. When the sample temperature reached 75 °C, the sample compartment was opened to the main vacuum chamber, releasing a burst of evolved products into the chamber. In this type of experiment, the only new peak compared to the blank silicon wafer occurred at m/z 44, assigned to CO₂ (Fig. S7). The peak at m/z 44 is not likely due to acetone. The electron impact mass spectrum of acetone has major peaks at m/z of 43 and 58 and only a small relative abundance (~2%) at m/z 44, ⁵⁵ and we did not observe m/z of 43 and 58 in our experiments. Therefore, it is unlikely that acetone is contributing significantly to the m/z 44 signal detected here.

The second type of experiment involved linearly heating the sample from -45 °C to 95 °C at a rate of 0.1 °C s⁻¹. During heating, the mass spectrometer was set for single ion monitoring at m/z 44, identified during the first experimental approach. The CO₂ signal at m/z 44 was observed to

increase starting at 40 °C and reach a maximum at 95 °C (Fig. 6a). The temperature was then held at 95 °C and the signal decreased back to the background level within 5 min (Fig. 6b). The onset temperature for the evolution of CO_2 here is consistent with the onset observed by imaging the particle's cross-sectional area (Fig. 1). When the same procedure was carried out with α -pinene SOA, the m/z 44 signal was much lower (Fig. 6a and 6b). For EI-MS measurements, the heating of SOA occurs at reduced pressures. This may have resulted in faster evaporation kinetics, compared to the other techniques used in this study; however, the onset temperature of decomposition was likely not strongly dependent on pressure.

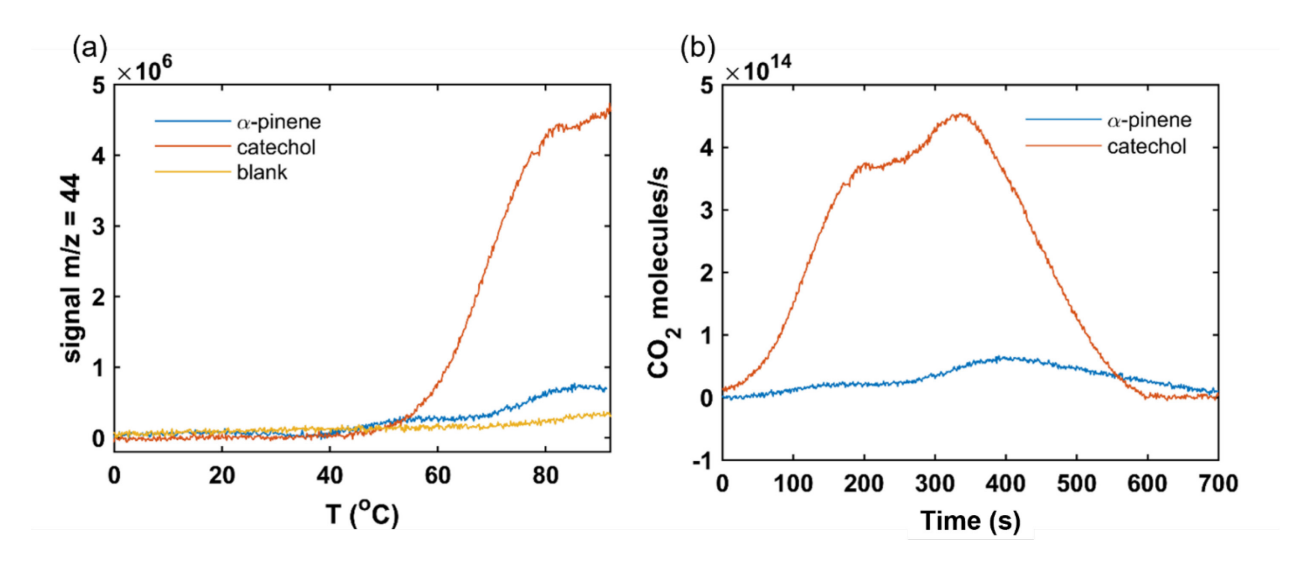


Figure 6. Panel (a): temperature response curves for m/z 44 during heating of α -pinene SOA (blue), catechol SOA (orange), and blank (yellow) samples. Panel (b): chromatogram showing the time evolution of the molecular flux of CO₂ during a temperature ramp for α -pinene SOA (blue) and catechol SOA (orange). Time zero indicates time of peak onset which corresponds to 40 °C and time 405 s corresponds to 95 °C.

Table 1. Calculation of CO₂ yield.

SOA type	SOA Mass (mg) ^a	Initial Molecules SOA ^b	Molecules CO ₂ evolved	CO ₂ Yield (%) (moles CO ₂ /moles
α -pinene + O ₃	0.56 ± 0.09	$(1.7 \pm 0.3) \times 10^{18}$	1.2×10 ¹⁶	$\frac{\text{SOA})}{0.7 \pm 0.1}$
$catechol + O_3$	0.36 ± 0.09	$(1.1 \pm 0.3) \times 10^{18}$	1.3×10^{17}	12 ± 2.9

^a Error based on upper and lower limits in chamber mass loading during sample collection on Si wafers.

The yield of CO_2 produced during the heating process was calculated by calibrating the signal at m/z 44 using known pressures of CO_2 . The CO_2 signals in the chromatogram (Fig. 6b) were integrated. The integrated signal represents the total CO_2 evolved from the SOA sample (Table 1) since all the CO_2 molecules evolved eventually reach the detector. The total number of SOA molecules initially present was calculated by using the estimated total mass of SOA impacted on

^b Assuming an average molecular weight of 200 g mol⁻¹ for both SOA samples.

the silicon wafer substrates and by assuming an average molar mass of 200 g mol $^{-1}$. ⁵⁶ By dividing the number of CO₂ molecules evolved by the total number of initial molecules we estimate a CO₂ yield to be $12 \pm 2.9\%$ for catechol SOA. For comparison, we estimated a CO₂ yield of $0.7 \pm 0.1\%$ for α -pinene SOA. We also estimated the yield of acetone produced during heating of catechol SOA (to 52 °C) from the Vocus experiments to be 0.0008%, based on an estimated sensitivity of 10,000 cps/ppb. This yield is significantly smaller than the calculated yield of CO₂ from the EI-MS experiments.

Related to these observations, Zhao et al. recently suggested that heating of highly functionalized organic aerosol at mild to moderate temperatures (45-100 °C) leads to the decomposition of oligomers and the formation of CO₂, CO, and H₂O.²² In addition, to explain results from thermal desorption instruments, Stark et al. assumed that heating SOA leads to the loss of carboxyl groups (-CO₂), carbonyl groups (-CO), and hydroxyl groups (-H₂O, assuming dehydration involving the loss of a hydroxyl group).¹⁸ Nevertheless, additional studies are needed to determine the mechanism of CO₂ production from catechol SOA.

3.4. Characterization of condensed phase SOA components using UHPLC-HESI-HRMS

UHPLC-HESI-HRMS analysis was conducted on unheated catechol SOA samples and catechol SOA heated for ~2 h at either 36 or 52 °C. Fig. 7 shows the integrated mass spectra (from 2-16 min of chromatographic elution), and Table S1 presents a summary of the most abundant peaks from the mass spectra as well as possible molecular assignments. Some of the peaks were identified as monoterpene and sesquiterpene oxidation products, likely from SOA experiments conducted in the same environmental chamber prior to catechol SOA production. See Section S4 for further discussion.

Despite these issues with contamination, we were able to determine that a dimer ($C_{12}H_{12}O_8$) was a major species in the catechol SOA, and this species most likely decomposed or reacted away when heated to 52 °C. Consistent with this observation, Zhao et al. recently showed that oligomers in highly functionalized organic aerosol decompose at mild to moderate temperatures (45-100 °C). Pillar-Little et al. also observed the formation of dimers due to indirect oxidation by in situ produced OH during the ozonolysis of catechol. However, their dimers had different molecular formulas than observed here, and a OH scavenger was used in the current studies, which should have limited OH concentrations. Additional studies are needed to determine the structure and mechanism for formation of the dimer observed in the current study.

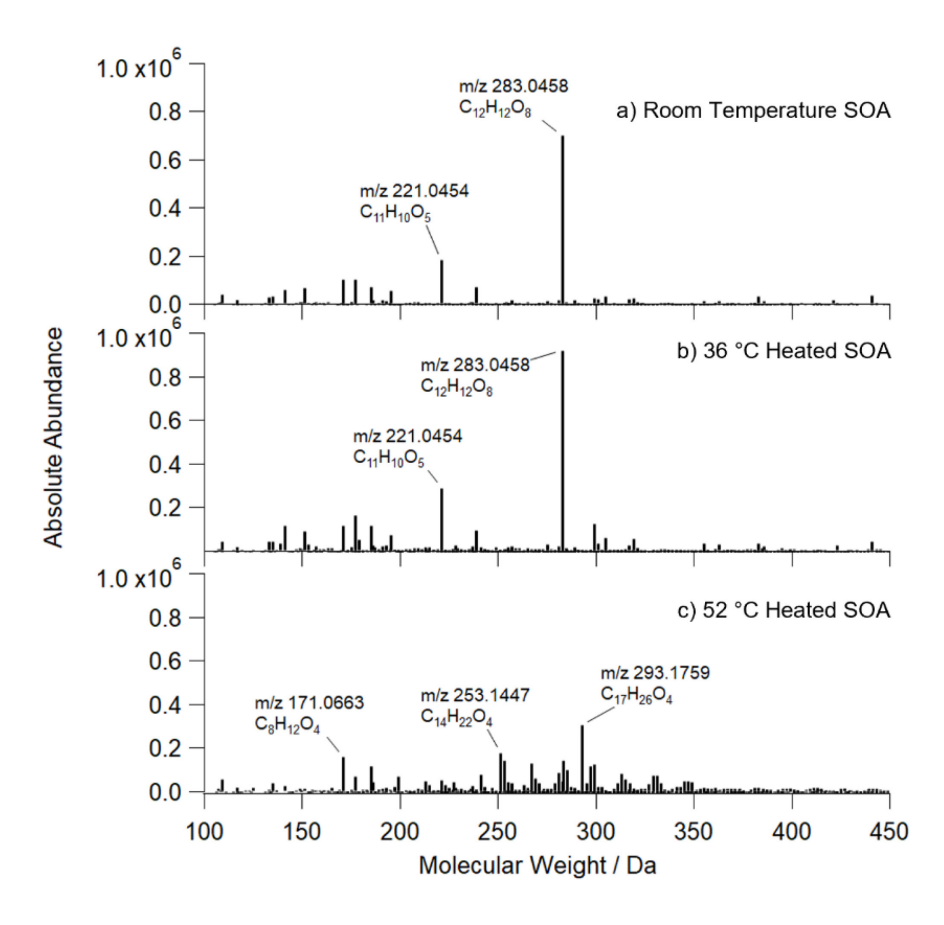


Figure. 7. Integrated high-resolution mass spectra for catechol SOA at (a) room temperature, (b) heated to 36 °C, and (c) heated to 52 °C. The peaks are shown with absolute abundance for each temperature.

3.5 Viscosity of SOA material and mixing time of CO2 within the SOA during heating

The viscosity of catechol SOA was previously measured to be $> 1 \times 10^9$ Pa s at 20 °C (293 K) under dry conditions, i.e., $\sim 0\%$ RH.³¹ We used these results and the Vogel-Fulcher-Tammann (VFT) equation to predict the viscosity of the catechol SOA at temperatures > 20 °C. The VFT equation describes the temperature dependence of viscosity:^{58,59}

$$\ln \eta(T) = \ln \eta_0 + \frac{D_f T_0}{T - T_0} \tag{1}$$

In eq. (1), η_0 is the viscosity at infinite temperature, $D_{\rm f}$ is the fragility parameter, and T_0 is the Vogel temperature. We assumed values of $D_{\rm f} = 10^{32,60-62}$ and $\eta_0 = 1 \times 10^{-5}.^{59}$ By inserting a viscosity of 1×10^9 Pa s and T = 20 °C (293 K) into Eq. 1, we calculated T_0 to be -49 °C for catechol SOA. Using this value for T_0 and our assumptions for $D_{\rm f}$ and η_0 , the viscosity of catechol SOA was predicted at temperatures > 20 °C (Fig. 8a). At temperatures of 36 and 52 °C, the viscosities were greater than 1×10^6 Pa s and 1×10^4 Pa s, respectively (Fig. 8a).

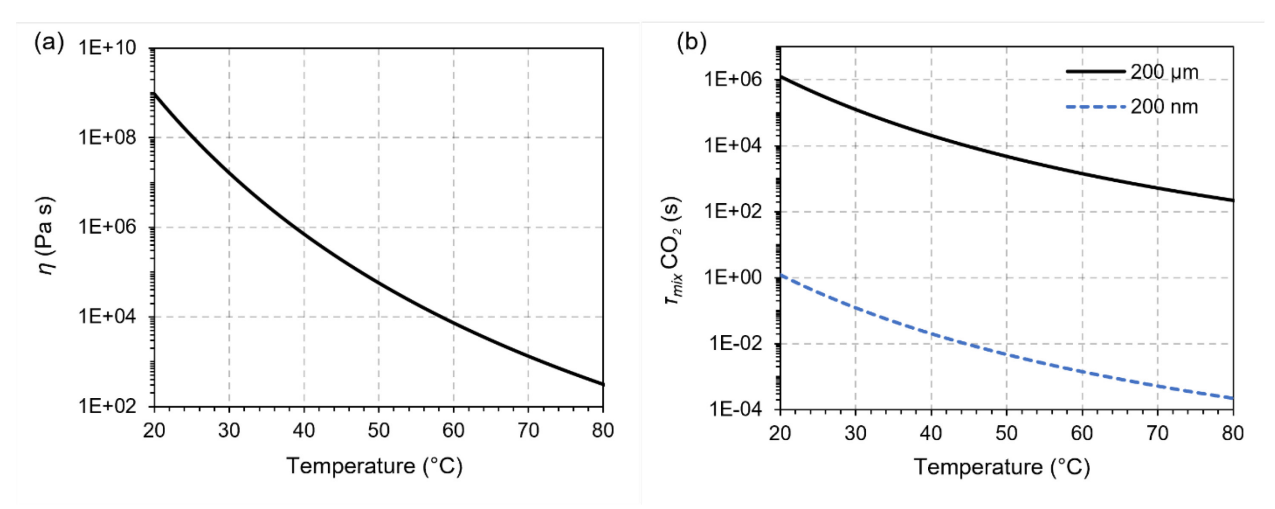


Figure 8. Panel (a): lower limits to the viscosity of catechol SOA as a function of temperature, calculated using the room temperature viscosity of catechol SOA from Kiland et al.³¹ with the VFT equation, eq. 1. Panel (b): the lower limits to the mixing time of CO_2 (τ_{mix} CO_2) in a 200 µm particle (black line) and a 200 nm particle (blue dashed line). Since the room temperature viscosities were lower limits, the viscosities and mixing times of CO_2 are lower limits.

From the viscosity results shown in Fig. 8a, we calculated the diffusion coefficient and mixing time of CO₂ within the SOA. The calculated diffusion coefficient and mixing time of CO₂ will be an upper limit to the diffusion coefficient and mixing time of acetone within the SOA since diffusion coefficients and mixing times are inversely related to the radius of the diffusion species. First, the diffusion coefficient of CO₂ within the SOA was calculated from viscosity using the fractional Stokes-Einstein equation:⁶³

$$D_{\text{CO2}}(T) = D_{\text{H2O}}^{\circ}(T) \times \left(\frac{\eta_{\text{H2O}}^{\circ}(T)}{\eta(T)}\right)^{\xi}$$
 (2)

where $D^{\circ}_{H2O}(T)$ is the temperature-dependent diffusion coefficient of water in pure water calculated with the Stokes-Einstein equation, and $\eta^{\circ}_{H2O}(T)$ is the temperature-dependent viscosity of pure water. $\eta^{\circ}_{H2O}(T)$ was calculated, as done previously, using a VFT fit to pure water viscosity data. $^{61,64,65}_{O}$ $\eta(T)$ is the viscosity in the SOA calculated with the VFT equation, and ξ is the fractional exponent determined by:

$$\xi = 1 - \left[A \times \exp\left(-B \frac{r_{\text{diff}}}{r_{\text{matrix}}}\right) \right] \tag{3}$$

where A and B are coefficients with values of 0.73 and 1.79, respectively. ⁶³ $r_{\rm diff}$ and $r_{\rm matrix}$ are the hydrodynamic radii of the diffusing molecules and matrix molecules, respectively. For CO₂, we used a $r_{\rm diff}$ of 0.103 nm. ⁶⁶ For $r_{\rm matrix}$, we used a value of 0.406 nm, based on the weighted average of the molecular weights shown in Table S1, an assumed spherical geometry of the matrix molecules, and a density of 1.4 g L⁻¹ for catechol SOA. ⁶⁷ A $r_{\rm matrix}$ of 0.406 nm yielded $\xi = 0.54$. The resulting diffusion coefficients of CO₂ were then used to calculate the mixing time of CO₂ within catechol SOA, using:

$$\tau_{\rm mix} = \frac{d_{\rm p}^{\,2}}{4\pi^2 D_{CO2}} \tag{4}$$

where d_p is the diameter of the catechol SOA particle and D_{CO2} is the diffusion coefficient of CO_2 in the SOA particles.

Shown in Fig. 8b (solid line) is the calculated mixing times as a function of temperature of CO_2 within a 200 µm particle (roughly the diameter of the supermicron particles observed using optical microscopy, which are the conglomerate of smaller aerosol particles). At temperatures of 36 and 52 °C, the mixing times of CO_2 within 200 µm catechol SOA particles are ~39600 and ~3640 s (11 and 1 h), respectively. Recall that these mixing times are based on a lower limit estimate of the viscosity of catechol at room temperature, so the mixing times here are also lower limits. The calculated mixing is relatively slow and these mixing times are longer than the experimental times used in the optical microscope experiments (Fig. 2 and 3). Hence, any CO_2 produced within a 200 µm particle during heating will not immediately escape the particles and could lead to the observed boiling behavior (see below).

3.6. Explanation of the boiling experiments

For boiling to occur in the SOA particles, two conditions must be fulfilled: (1) chemical reactions resulting in a formation of molecules with vapor pressures > 1 atm must occur when SOA is heated; (2) the production rate of these high vapor pressure molecules must be larger than the loss rate of these molecules by molecular diffusion of the molecules to the surface of the SOA particles followed by evaporation. The vapor pressure of acetone is < 1 atm at 36 and 52 °C.⁶⁸ The vapor pressure of CO₂ is >> 1 atm at these temperatures.^{69,70} Hence, the formation of CO₂ upon heating the SOA would satisfy the first criterion. The slow mixing time of CO₂ in the particles calculated above (Fig. 8b) also suggests that the second criterion would be satisfied in our experiments. Taken together, the formation of CO₂ during mild heating and the slow mixing time of CO₂ within the supermicron SOA particles explains the observed particle boiling behavior.

This is the first study that has directly observed boiling in SOA material due to heating. However, previous studies indirectly observed similar behavior. Specifically, Liang et al. observed the formation of inclusions/bubbles within supermicron particles containing ammonium nitrate and sucrose exposed to UV light. Liang et al. suggested the formation of inclusions/bubbles could be due to: 1) the fast production rate of NO₂ and NO by photolysis of ammonium nitrate; 2) the slow loss rate of NO₂ and NO by molecular diffusion to the surface of the particles followed by evaporation. These arguments are very similar to the explanations presented in this work. In general, we expect that inclusions/bubbles are expected in supermicron particles during heating or photolysis if there is fast production of high volatility compounds (e.g., NO₂, CO₂) and high material viscosities, which limits the loss rate of these high volatility compounds.

3.7 Extrapolation to submicron SOA particles

Our experiments were carried out with supermicron particles (conglomerated SOA particles with diameters of ~200 μ m in the optical microscopy experiments). For this case, the mixing time of CO₂ within the particles is long, even at 36 and 52 °C (> 1 h) (Fig. 8b, solid line).

We have also calculated lower limits to the mixing time of CO₂ in 200 nm SOA particles as a function of temperature (Fig. 8b, dashed line) using Eq. 2–4. 200 nm particles were used for these calculations since they approximately correspond to the median diameter of an accumulation mode particle in the troposphere.⁷² In this case, the lower limits to the mixing times were 0.04 and 0.004 s at 36 and 52 °C, respectively. If the mixing time of CO₂ is 0.04 to 0.004 s, any CO₂ produced in the particles during heating would very quickly escape the particles, and boiling would not be expected. However, the mixing times could be larger than 0.04 and 0.004 s since our calculated mixing times correspond to lower limits. As a result, we are not able to rule out boiling in 200 nm catechol SOA particles during heating. Additional experiments are needed to better constrain the viscosity and mixing times of CO₂ at warm temperatures to determine if boiling can occur in 200 nm catechol SOA at mild heating temperatures.

3.8 Implications

We have shown that mild heating of catechol SOA causes acetone and CO₂ production resulting from the decomposition of SOA compounds. The production of acetone and CO₂ during heating coupled with the high viscosity of the catechol SOA have implications for extracting the volatilities of SOA components from thermograms. The production of acetone and CO₂ implies fragmentation reactions of SOA components when heating, which will need to be considered when analyzing thermograms of catechol SOA and potentially other SOA materials where similar reactions and processes can occur.

The high viscosities of the SOA should similarly be considered when analyzing TD measurements. When converting TD measurements to volatilities, researchers have often assumed that the SOA particles are well mixed, implying their viscosity is low and not a kinetic barrier to evaporation. 11,12,30 For most TD measurements, particle diameters are on the order of 200 nm. We calculated lower limits to viscosities and mixing times within 200 nm catechol SOA as a function of temperature (Fig. 8). However, we are not able to determine if 200 nm catechol SOA particles will be well mixed in TD measurements when heated to mild temperatures since the calculations were lower limits. For some TD measurements, sub-micrometer SOA particles are first collected on a surface using an impactor. 20 If particle collection times are long and particle mass loadings are high, sub-micrometer SOA particles will coagulate on the surface and form particles with dimensions greater than 1 μ m. If the particle dimensions reach \sim 200 μ m, the SOA particles will not be well mixed in TD measurements when heated to mild temperatures based on our calculations (Fig. 8).

We have also shown here that optical microscopy combined with a heating stage is a simple and sensitive method for determining cases when 1) molecules with high vapor pressures (> 1 atm) are produced by thermal decomposition and 2) the viscosity of the particles is high even when heated. It would be instructive to apply this technique to other types of SOA of atmospheric importance.

Supporting Information

The Supporting Information contains relevant chemical structures, schematics of the imaging experiments, additional mass spectrometry data, a discussion of possible contamination from other SOA experiments, and videos captured of catechol SOA boiling.

Acknowledgments

This work was supported by the Natural Sciences and Engineering Research Council of Canada through grant RGPIN/2023-05333 (K.J.K., F.M., S.N., and A.K.B.), the Canada Foundation for Innovation's John R. Evans Leaders Fund (A.A.A. and N.B.) and US National Science Foundation Grants No. AGS-1853639 (K.S.H. and S.A.N.) and AGS-2030175 (K.N.J., Y.L., and B.J.F).

References

- (1) Akherati, A.; He, Y.; Coggon, M. M.; Koss, A. R.; Hodshire, A. L.; Sekimoto, K.; Warneke, C.; de Gouw, J.; Yee, L.; Seinfeld, J. H.; Onasch, T. B.; Herndon, S. C.; Knighton, W. B.; Cappa, C. D.; Kleeman, M. J.; Lim, C. Y.; Kroll, J. H.; Pierce, J. R.; Jathar, S. H. Oxygenated Aromatic Compounds Are Important Precursors of Secondary Organic Aerosol in Biomass-Burning Emissions. *Environ. Sci. Technol.* **2020**, *54* (14), 8568–8579. https://doi.org/10.1021/acs.est.0c01345.
- (2) Decker, Z. C. J.; Robinson, M. A.; Barsanti, K. C.; Bourgeois, I.; Coggon, M. M.; DiGangi, J. P.; Diskin, G. S.; Flocke, F. M.; Franchin, A.; Fredrickson, C. D.; Gkatzelis, G. I.; Hall, S. R.; Halliday, H.; Holmes, C. D.; Huey, L. G.; Lee, Y. R.; Lindaas, J.; Middlebrook, A. M.; Montzka, D. D.; Moore, R.; Neuman, J. A.; Nowak, J. B.; Palm, B. B.; Peischl, J.; Piel, F.; Rickly, P. S.; Rollins, A. W.; Ryerson, T. B.; Schwantes, R. H.; Sekimoto, K.; Thornhill, L.; Thornton, J. A.; Tyndall, G. S.; Ullmann, K.; Van Rooy, P.; Veres, P. R.; Warneke, C.; Washenfelder, R. A.; Weinheimer, A. J.; Wiggins, E.; Winstead, E.; Wisthaler, A.; Womack, C.; Brown, S. S. Nighttime and Daytime Dark Oxidation Chemistry in Wildfire Plumes: An Observation and Model Analysis of FIREX-AQ Aircraft Data. Atmos. Chem. Phys. 2021, 21 (21), 16293–16317. https://doi.org/10.5194/acp-21-16293-2021.
- (3) Mazzoleni, L. R.; Zielinska, B.; Moosmüller, H. Emissions of Levoglucosan, Methoxy Phenols, and Organic Acids from Prescribed Burns, Laboratory Combustion of Wildland Fuels, and Residential Wood Combustion. *Environ. Sci. Technol.* **2007**, *41* (7), 2115–2122. https://doi.org/10.1021/es061702c.
- (4) Shrivastava, M.; Easter, R. C.; Liu, X.; Zelenyuk, A.; Singh, B.; Zhang, K.; Ma, P.-L.; Chand, D.; Ghan, S.; Jimenez, J. L.; Zhang, Q.; Fast, J.; Rasch, P. J.; Tiitta, P. Global Transformation and Fate of SOA: Implications of Low-Volatility SOA and Gas-Phase Fragmentation Reactions. *J. Geophys. Res. Atmos.* **2015**, *120* (9), 4169–4195. https://doi.org/10.1002/2014JD022563.
- (5) Ervens, B.; Turpin, B. J.; Weber, R. J. Secondary Organic Aerosol Formation in Cloud Droplets and Aqueous Particles (AqSOA): A Review of Laboratory, Field and Model

- Studies. Atmos. Chem. Phys. **2011**, 11 (21), 11069–11102. https://doi.org/10.5194/acp-11-11069-2011.
- (6) Coeur-Tourneur, C.; Tomas, A.; Guilloteau, A.; Henry, F.; Ledoux, F.; Visez, N.; Riffault, V.; Wenger, J. C.; Bedjanian, Y. Aerosol Formation Yields from the Reaction of Catechol with Ozone. *Atmos. Environ.* **2009**, *43* (14), 2360–2365. https://doi.org/10.1016/j.atmosenv.2008.12.054.
- (7) Pillar-Little, E. A.; Camm, R. C.; Guzman, M. I. Catechol Oxidation by Ozone and Hydroxyl Radicals at the Air–Water Interface. *Environ. Sci. Technol.* **2014**, *48* (24), 14352–14360. https://doi.org/10.1021/es504094x.
- (8) Arciva, S.; Niedek, C.; Mavis, C.; Yoon, M.; Sanchez, M. E.; Zhang, Q.; Anastasio, C. Aqueous · OH Oxidation of Highly Substituted Phenols as a Source of Secondary Organic Aerosol. *Environ. Sci. Technol.* **2022**, *56* (14), 9959–9967. https://doi.org/10.1021/acs.est.2c02225.
- (9) Shiraiwa, M.; Ueda, K.; Pozzer, A.; Lammel, G.; Kampf, C. J.; Fushimi, A.; Enami, S.; Arangio, A. M.; Fröhlich-Nowoisky, J.; Fujitani, Y.; Furuyama, A.; Lakey, P. S. J.; Lelieveld, J.; Lucas, K.; Morino, Y.; Pöschl, U.; Takahama, S.; Takami, A.; Tong, H.; Weber, B.; Yoshino, A.; Sato, K. Aerosol Health Effects from Molecular to Global Scales. *Environ. Sci. Technol.* **2017**, *51* (23), 13545–13567. https://doi.org/10.1021/acs.est.7b04417.
- (10) Forster, P.; T. Storelvmo; K. Armour; W. Collins; J.-L. Dufresne; D. Frame; D.J. Lunt; T. Mauritsen; M.D. Palmer; M. Watanabe; M. Wild; H. Zhang. The Earth's Energy Budget, Climate Feedbacks and Climate Sensitivity. In *Climate Change 2021 The Physical Science Basis*; Cambridge University Press, 2023; pp 923–1054. https://doi.org/10.1017/9781009157896.009.
- (11) Cappa, C. D.; Wilson, K. R. Evolution of Organic Aerosol Mass Spectra upon Heating: Implications for OA Phase and Partitioning Behavior. *Atmos. Chem. Phys.* **2011**, *11* (5), 1895–1911. https://doi.org/10.5194/acp-11-1895-2011.
- (12) Cappa, C. D.; Jimenez, J. L. Quantitative Estimates of the Volatility of Ambient Organic Aerosol. *Atmos. Chem. Phys.* **2010**, *10* (12), 5409–5424. https://doi.org/10.5194/acp-10-5409-2010.
- (13) Smith, J. N.; Moore, K. F.; McMurry, P. H.; Eisele, F. L. Atmospheric Measurements of Sub-20 Nm Diameter Particle Chemical Composition by Thermal Desorption Chemical Ionization Mass Spectrometry. *Aerosol Sci. Technol.* 2004, 38 (2), 100–110. https://doi.org/10.1080/02786820490249036.
- (14) Holzinger, R.; Williams, J.; Herrmann, F.; Lelieveld, J.; Donahue, N. M.; Röckmann, T. Aerosol Analysis Using a Thermal-Desorption Proton-Transfer-Reaction Mass Spectrometer (TD-PTR-MS): A New Approach to Study Processing of Organic Aerosols. *Atmos. Chem. Phys.* **2010**, *10* (5), 2257–2267. https://doi.org/10.5194/acp-10-2257-2010.
- (15) Zhang, H.; Yee, L. D.; Lee, B. H.; Curtis, M. P.; Worton, D. R.; Isaacman-VanWertz, G.; Offenberg, J. H.; Lewandowski, M.; Kleindienst, T. E.; Beaver, M. R.; Holder, A. L.; Lonneman, W. A.; Docherty, K. S.; Jaoui, M.; Pye, H. O. T.; Hu, W.; Day, D. A.;

- Campuzano-Jost, P.; Jimenez, J. L.; Guo, H.; Weber, R. J.; de Gouw, J.; Koss, A. R.; Edgerton, E. S.; Brune, W.; Mohr, C.; Lopez-Hilfiker, F. D.; Lutz, A.; Kreisberg, N. M.; Spielman, S. R.; Hering, S. V.; Wilson, K. R.; Thornton, J. A.; Goldstein, A. H. Monoterpenes Are the Largest Source of Summertime Organic Aerosol in the Southeastern United States. *Proc. Natl. Acad. Sci.* **2018**, *115* (9), 2038–2043. https://doi.org/10.1073/pnas.1717513115.
- (16) Cain, K. P.; Karnezi, E.; Pandis, S. N. Challenges in Determining Atmospheric Organic Aerosol Volatility Distributions Using Thermal Evaporation Techniques. *Aerosol Sci. Technol.* **2020**, *54* (8), 941–957. https://doi.org/10.1080/02786826.2020.1748172.
- (17) Voliotis, A.; Wang, Y.; Shao, Y.; Du, M.; Bannan, T. J.; Percival, C. J.; Pandis, S. N.; Alfarra, M. R.; McFiggans, G. Exploring the Composition and Volatility of Secondary Organic Aerosols in Mixed Anthropogenic and Biogenic Precursor Systems. *Atmos. Chem. Phys.* **2021**, *21* (18), 14251–14273. https://doi.org/10.5194/acp-21-14251-2021.
- (18) Stark, H.; Yatavelli, R. L. N.; Thompson, S. L.; Kang, H.; Krechmer, J. E.; Kimmel, J. R.; Palm, B. B.; Hu, W.; Hayes, P. L.; Day, D. A.; Campuzano-Jost, P.; Canagaratna, M. R.; Jayne, J. T.; Worsnop, D. R.; Jimenez, J. L. Impact of Thermal Decomposition on Thermal Desorption Instruments: Advantage of Thermogram Analysis for Quantifying Volatility Distributions of Organic Species. *Environ. Sci. Technol.* **2017**, *51* (15), 8491–8500. https://doi.org/10.1021/acs.est.7b00160.
- (19) Claflin, M. S.; Ziemann, P. J. Thermal Desorption Behavior of Hemiacetal, Acetal, Ether, and Ester Oligomers. *Aerosol Sci. Technol.* **2019**, *53* (4), 473–484. https://doi.org/10.1080/02786826.2019.1576853.
- (20) Yatavelli, R. L. N.; Lopez-Hilfiker, F.; Wargo, J. D.; Kimmel, J. R.; Cubison, M. J.; Bertram, T. H.; Jimenez, J. L.; Gonin, M.; Worsnop, D. R.; Thornton, J. A. A Chemical Ionization High-Resolution Time-of-Flight Mass Spectrometer Coupled to a Micro Orifice Volatilization Impactor (MOVI-HRToF-CIMS) for Analysis of Gas and Particle-Phase Organic Species. *Aerosol Sci. Technol.* 2012, 46 (12), 1313–1327. https://doi.org/10.1080/02786826.2012.712236.
- (21) Huang, Y.; Kenseth, C. M.; Dalleska, N. F.; Seinfeld, J. H. Coupling Filter-Based Thermal Desorption Chemical Ionization Mass Spectrometry with Liquid Chromatography/Electrospray Ionization Mass Spectrometry for Molecular Analysis of Secondary Organic Aerosol. *Environ. Sci. Technol.* **2020**, *54* (20), 13238–13248. https://doi.org/10.1021/acs.est.0c01779.
- (22) Zhao, Z.; Yang, X.; Lee, J.; Tolentino, R.; Mayorga, R.; Zhang, W.; Zhang, H. Diverse Reactions in Highly Functionalized Organic Aerosols during Thermal Desorption. ACS Earth Sp. Chem. 2020, 4 (2), 283–296. https://doi.org/10.1021/acsearthspacechem.9b00312.
- (23) D'Ambro, E. L.; Schobesberger, S.; Zaveri, R. A.; Shilling, J. E.; Lee, B. H.; Lopez-Hilfiker, F. D.; Mohr, C.; Thornton, J. A. Isothermal Evaporation of α-Pinene Ozonolysis SOA: Volatility, Phase State, and Oligomeric Composition. *ACS Earth Sp. Chem.* **2018**, *2* (10), 1058–1067. https://doi.org/10.1021/acsearthspacechem.8b00084.

- (24) Lopez-Hilfiker, F. D.; Mohr, C.; Ehn, M.; Rubach, F.; Kleist, E.; Wildt, J.; Mentel, T. F.; Lutz, A.; Hallquist, M.; Worsnop, D.; Thornton, J. A. A Novel Method for Online Analysis of Gas and Particle Composition: Description and Evaluation of a Filter Inlet for Gases and AEROsols (FIGAERO). *Atmos. Meas. Tech.* 2014, 7 (4), 983–1001. https://doi.org/10.5194/amt-7-983-2014.
- (25) Hall, W. A.; Johnston, M. V. The Thermal-Stability of Oligomers in Alpha-Pinene Secondary Organic Aerosol. *Aerosol Sci. Technol.* **2012**, *46* (9), 983–989. https://doi.org/10.1080/02786826.2012.685114.
- (26) Lopez-Hilfiker, F. D.; Mohr, C.; D'Ambro, E. L.; Lutz, A.; Riedel, T. P.; Gaston, C. J.; Iyer, S.; Zhang, Z.; Gold, A.; Surratt, J. D.; Lee, B. H.; Kurten, T.; Hu, W. W.; Jimenez, J.; Hallquist, M.; Thornton, J. A. Molecular Composition and Volatility of Organic Aerosol in the Southeastern U.S.: Implications for IEPOX Derived SOA. *Environ. Sci. Technol.* 2016, 50 (5), 2200–2209. https://doi.org/10.1021/acs.est.5b04769.
- D'Ambro, E. L.; Schobesberger, S.; Gaston, C. J.; Lopez-Hilfiker, F. D.; Lee, B. H.; Liu, J.; Zelenyuk, A.; Bell, D.; Cappa, C. D.; Helgestad, T.; Li, Z.; Guenther, A.; Wang, J.; Wise, M.; Caylor, R.; Surratt, J. D.; Riedel, T.; Hyttinen, N.; Salo, V.-T.; Hasan, G.; Kurtén, T.; Shilling, J. E.; Thornton, J. A. Chamber-Based Insights into the Factors Controlling Epoxydiol (IEPOX) Secondary Organic Aerosol (SOA) Yield, Composition, and Volatility. Atmos. Chem. Phys. 2019, 19 (17), 11253–11265. https://doi.org/10.5194/acp-19-11253-2019.
- (28) DePalma, J. W.; Horan, A. J.; Hall IV, W. A.; Johnston, M. V. Thermodynamics of Oligomer Formation: Implications for Secondary Organic Aerosol Formation and Reactivity. *Phys. Chem. Chem. Phys.* **2013**, *15* (18), 6935–6943. https://doi.org/10.1039/c3cp44586k.
- (29) Finewax, Z.; de Gouw, J. A.; Ziemann, P. J. Identification and Quantification of 4-Nitrocatechol Formed from OH and NO3 Radical-Initiated Reactions of Catechol in Air in the Presence of NOx: Implications for Secondary Organic Aerosol Formation from Biomass Burning. *Environ. Sci. Technol.* **2018**, *52* (4), 1981–1989. https://doi.org/10.1021/acs.est.7b05864.
- (30) Schobesberger, S.; D'Ambro, E. L.; Lopez-Hilfiker, F. D.; Mohr, C.; Thornton, J. A. A Model Framework to Retrieve Thermodynamic and Kinetic Properties of Organic Aerosol from Composition-Resolved Thermal Desorption Measurements. *Atmos. Chem. Phys.* **2018**, *18* (20), 14757–14785. https://doi.org/10.5194/acp-18-14757-2018.
- (31) Kiland, K. J.; Mahrt, F.; Peng, L.; Nikkho, S.; Zaks, J.; Crescenzo, G. V.; Bertram, A. K. Viscosity, Glass Formation, and Mixing Times within Secondary Organic Aerosol from Biomass Burning Phenolics. *ACS Earth Sp. Chem.* **2023**, *7* (7), 1388–1400. https://doi.org/10.1021/acsearthspacechem.3c00039.
- (32) Maclean, A. M.; Smith, N. R.; Li, Y.; Huang, Y.; Hettiyadura, A. P. S.; Crescenzo, G. V.; Shiraiwa, M.; Laskin, A.; Nizkorodov, S. A.; Bertram, A. K. Humidity-Dependent Viscosity of Secondary Organic Aerosol from Ozonolysis of β-Caryophyllene: Measurements, Predictions, and Implications. ACS Earth Sp. Chem. 2021, 5 (2), 305–318. https://doi.org/10.1021/acsearthspacechem.0c00296.

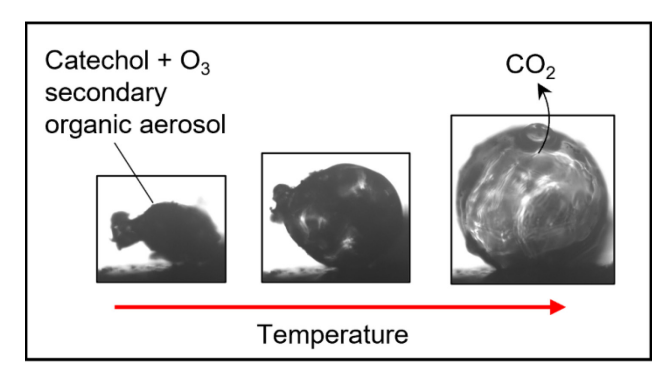
- (33) Smith, N. R.; Crescenzo, G. V.; Huang, Y.; Hettiyadura, A. P. S.; Siemens, K.; Li, Y.; Faiola, C. L.; Laskin, A.; Shiraiwa, M.; Bertram, A. K.; Nizkorodov, S. A. Viscosity and Liquid–Liquid Phase Separation in Healthy and Stressed Plant SOA. *Environ. Sci. Atmos.* **2021**, *1* (3), 140–153. https://doi.org/10.1039/d0ea00020e.
- Yli-Juuti, T.; Pajunoja, A.; Tikkanen, O. P.; Buchholz, A.; Faiola, C.; Väisänen, O.; Hao, L.; Kari, E.; Peräkylä, O.; Garmash, O.; Shiraiwa, M.; Ehn, M.; Lehtinen, K.; Virtanen, A. Factors Controlling the Evaporation of Secondary Organic Aerosol from α-Pinene Ozonolysis. *Geophys. Res. Lett.* 2017, 44 (5), 2562–2570. https://doi.org/10.1002/2016GL072364.
- (35) Zhang, Y.; Sanchez, M. S.; Douet, C.; Wang, Y.; Bateman, A. P.; Gong, Z.; Kuwata, M.; Renbaum-Wolff, L.; Sato, B. B.; Liu, P. F.; Bertram, A. K.; Geiger, F. M.; Martin, S. T. Changing Shapes and Implied Viscosities of Suspended Submicron Particles. *Atmos. Chem. Phys.* 2015, 15 (14), 7819–7829. https://doi.org/10.5194/acp-15-7819-2015.
- (36) Reid, J. P.; Bertram, A. K.; Topping, D. O.; Laskin, A.; Martin, S. T.; Petters, M. D.; Pope, F. D.; Rovelli, G. The Viscosity of Atmospherically Relevant Organic Particles. *Nat. Commun.* **2018**, *9* (956), 1–14. https://doi.org/10.1038/s41467-018-03027-z.
- (37) Baboomian, V. J.; Crescenzo, G. V; Huang, Y.; Mahrt, F.; Shiraiwa, M.; Bertram, A. K.; Nizkorodov, S. A. Sunlight Can Convert Atmospheric Aerosols into a Glassy Solid State and Modify Their Environmental Impacts. *Proc. Natl. Acad. Sci.* **2022**, *119* (43), 1–10. https://doi.org/10.1073/pnas.2208121119.
- (38) Lei, Z.; Olson, N. E.; Zhang, Y.; Chen, Y.; Lambe, A. T.; Zhang, J.; White, N. J.; Atkin, J. M.; Banaszak Holl, M. M.; Zhang, Z.; Gold, A.; Surratt, J. D.; Ault, A. P. Morphology and Viscosity Changes after Reactive Uptake of Isoprene Epoxydiols in Submicrometer Phase Separated Particles with Secondary Organic Aerosol Formed from Different Volatile Organic Compounds. ACS Earth Sp. Chem. 2022, 6 (4), 871–882. https://doi.org/10.1021/acsearthspacechem.1c00156.
- (39) Kidd, C.; Perraud, V.; Wingen, L. M.; Finlayson-Pitts, B. J. Integrating Phase and Composition of Secondary Organic Aerosol from the Ozonolysis of α-Pinene. *Proc. Natl. Acad. Sci.* **2014**, *111* (21), 7552–7557. https://doi.org/10.1073/pnas.1322558111.
- (40) Morino, Y.; Sato, K.; Jathar, S. H.; Tanabe, K.; Inomata, S.; Fujitani, Y.; Ramasamy, S.; Cappa, C. D. Modeling the Effects of Dimerization and Bulk Diffusion on the Evaporative Behavior of Secondary Organic Aerosol Formed from α-Pinene and 1,3,5-Trimethylbenzene. ACS Earth Sp. Chem. 2020, 4 (11), 1931–1946. https://doi.org/10.1021/acsearthspacechem.0c00106.
- (41) Petters, S. S.; Kreidenweis, S. M.; Grieshop, A. P.; Ziemann, P. J.; Petters, M. D. Temperature- and Humidity-Dependent Phase States of Secondary Organic Aerosols. *Geophys. Res. Lett.* **2019**, *46* (2), 1005–1013. https://doi.org/10.1029/2018GL080563.
- (42) Kiland, K. J.; Marroquin, K. L.; Smith, N. R.; Xu, S.; Nizkorodov, S. A.; Bertram, A. K. A New Hot-Stage Microscopy Technique for Measuring Temperature-Dependent Viscosities of Aerosol Particles and Its Application to Farnesene Secondary Organic Aerosol. *Atmos. Meas. Tech.* 2022, 15 (19), 5545–5561. https://doi.org/10.5194/amt-15-

- 5545-2022.
- (43) Qin, Y.; Ye, J.; Ohno, P.; Nah, T.; T. Martin, S. Temperature-Dependent Viscosity of Organic Materials Characterized by Atomic Force Microscope. *Atmosphere (Basel)*. **2021**, *12* (11), 1476. https://doi.org/10.3390/atmos12111476.
- (44) Lei, Z.; Zhang, J.; Mueller, E. A.; Xiao, Y.; Kolozsvari, K. R.; McNeil, A. J.; Banaszak Holl, M. M.; Ault, A. P. Glass Transition Temperatures of Individual Submicrometer Atmospheric Particles: Direct Measurement via Heated Atomic Force Microscopy Probe. *Anal. Chem.* **2022**, *94* (35), 11973–11977. https://doi.org/10.1021/acs.analchem.2c01979.
- (45) Sun, J.; Mei, Q.; Wei, B.; Huan, L.; Xie, J.; He, M. Mechanisms for Ozone-Initiated Removal of Biomass Burning Products from the Atmosphere. *Environ. Chem.* **2018**, *15* (2), 83. https://doi.org/10.1071/EN17212.
- (46) Barnum, T. J.; Medeiros, N.; Hinrichs, R. Z. Condensed-Phase versus Gas-Phase Ozonolysis of Catechol: A Combined Experimental and Theoretical Study. *Atmos. Environ.* **2012**, *55*, 98–106. https://doi.org/10.1016/j.atmosenv.2012.02.019.
- (47) Huang, Y.; Mahrt, F.; Xu, S.; Shiraiwa, M.; Zuend, A.; Bertram, A. K. Coexistence of Three Liquid Phases in Individual Atmospheric Aerosol Particles. *Proc. Natl. Acad. Sci. U. S. A.* **2021**, *118* (16), e2102512118. https://doi.org/10.1073/pnas.2102512118.
- (48) Cavalli, F.; Geiger, H.; Barnes, I.; Becker, K. H. FTIR Kinetic, Product, and Modeling Study of the OH-Initiated Oxidation of 1-Butanol in Air. *Environ. Sci. Technol.* **2002**, *36* (6), 1263–1270. https://doi.org/10.1021/es010220s.
- (49) Kiland, K. J.; Maclean, A. M.; Kamal, S.; Bertram, A. K. Diffusion of Organic Molecules as a Function of Temperature in a Sucrose Matrix (a Proxy for Secondary Organic Aerosol). *J. Phys. Chem. Lett.* **2019**, *10* (19), 5902–5908. https://doi.org/10.1021/acs.jpclett.9b02182.
- (50) Krechmer, J.; Lopez-Hilfiker, F.; Koss, A.; Hutterli, M.; Stoermer, C.; Deming, B.; Kimmel, J.; Warneke, C.; Holzinger, R.; Jayne, J.; Worsnop, D.; Fuhrer, K.; Gonin, M.; de Gouw, J. Evaluation of a New Reagent-Ion Source and Focusing Ion–Molecule Reactor for Use in Proton-Transfer-Reaction Mass Spectrometry. *Anal. Chem.* **2018**, *90* (20), 12011–12018. https://doi.org/10.1021/acs.analchem.8b02641.
- (51) Jensen, A. R.; Koss, A. R.; Hales, R. B.; de Gouw, J. A. Measurements of Volatile Organic Compounds in Ambient Air by Gas-Chromatography and Real-Time Vocus PTR-TOF-MS: Calibrations, Instrument Background Corrections, and Introducing a PTR Data Toolkit. Atmos. Meas. Tech. 2023, 16 (21), 5261–5285. https://doi.org/10.5194/amt-16-5261-2023.
- (52) Malecha, K. T.; Cai, Z.; Nizkorodov, S. A. Photodegradation of Secondary Organic Aerosol Material Quantified with a Quartz Crystal Microbalance. *Environ. Sci. Technol. Lett.* **2018**, *5* (6), 366–371. https://doi.org/10.1021/acs.estlett.8b00231.
- (53) Malecha, K. T.; Nizkorodov, S. A. Photodegradation of Secondary Organic Aerosol Particles as a Source of Small, Oxygenated Volatile Organic Compounds. *Environ. Sci. Technol.* **2016**, *50* (18), 9990–9997. https://doi.org/10.1021/acs.est.6b02313.

- (54) Moldoveanu, S. C. Pyrolysis of Organic Molecules with Applications to Health and Environmental Issues; Elsevier B.V. Netherlands, 2010; pp 343, 512. https://doi.org/10.1016/S0167-9244(09)02830-3.
- (55) NIST Chemistry WebBook, SRD 69. https://webbook.nist.gov/cgi/cbook.cgi?ID=C67641&Mask=200#Mass-Spec (accessed 2024-03-21).
- (56) Williams, B. J.; Goldstein, A. H.; Kreisberg, N. M.; Hering, S. V. In Situ Measurements of Gas/Particle-Phase Transitions for Atmospheric Semivolatile Organic Compounds. *Proc. Natl. Acad. Sci.* **2010**, *107* (15), 6676–6681. https://doi.org/10.1073/pnas.0911858107.
- (57) Pillar-Little, E. A.; Zhou, R.; Guzman, M. I. Heterogeneous Oxidation of Catechol. *J. Phys. Chem. A* **2015**, *119* (41), 10349–10359. https://doi.org/10.1021/acs.jpca.5b07914.
- (58) Fulcher, G. S. Analysis of Recent Measurements of the Viscosity of Glasses. *J. Am. Ceram. Soc.* **1925**, 8 (6), 339–355. https://doi.org/10.1111/j.1151-2916.1992.tb05536.x.
- (59) Angell, C. . Relaxation in Liquids, Polymers and Plastic Crystals Strong/Fragile Patterns and Problems. *J. Non. Cryst. Solids* **1991**, *131–133* (PART 1), 13–31. https://doi.org/10.1016/0022-3093(91)90266-9.
- (60) Shiraiwa, M.; Li, Y.; Tsimpidi, A. P.; Karydis, V. A.; Berkemeier, T.; Pandis, S. N.; Lelieveld, J.; Koop, T.; Pöschl, U. Global Distribution of Particle Phase State in Atmospheric Secondary Organic Aerosols. *Nat. Commun.* **2017**, *8* (1), 15002. https://doi.org/10.1038/ncomms15002.
- (61) Maclean, A. M.; Li, Y.; Crescenzo, G. V.; Smith, N. R.; Karydis, V. A.; Tsimpidi, A. P.; Butenhoff, C. L.; Faiola, C. L.; Lelieveld, J.; Nizkorodov, S. A.; Shiraiwa, M.; Bertram, A. K. Global Distribution of the Phase State and Mixing Times within Secondary Organic Aerosol Particles in the Troposphere Based on Room-Temperature Viscosity Measurements. ACS Earth Sp. Chem. 2021, 5 (12), 3458–3473. https://doi.org/10.1021/acsearthspacechem.1c00296.
- (62) Gervasi, N. R.; Topping, D. O.; Zuend, A. A Predictive Group-Contribution Model for the Viscosity of Aqueous Organic Aerosol. *Atmos. Chem. Phys.* **2020**, *20* (5), 2987–3008. https://doi.org/10.5194/acp-20-2987-2020.
- (63) Evoy, E.; Kamal, S.; Patey, G. N.; Martin, S. T.; Bertram, A. K. Unified Description of Diffusion Coefficients from Small to Large Molecules in Organic-Water Mixtures. *J. Phys. Chem. A* **2020**, *124* (11), 2301–2308. https://doi.org/10.1021/acs.jpca.9b11271.
- (64) Crittenden, J. C.; Trussell, R. R.; Hand, D. W.; Howe, K. J.; Tchobanoglous, G. *MWH's Water Treatment*; John Wiley & Sons, Inc., 2012. https://doi.org/10.1002/9781118131473.
- (65) Hallett, J. The Temperature Dependence of the Viscosity of Supercooled Water. *Proc. Phys. Soc.* **1963**, *82* (6), 1046–1050. https://doi.org/10.1088/0370-1328/82/6/326.
- (66) Ahmed Khaireh, M.; Angot, M.; Cilindre, C.; Liger-Belair, G.; Bonhommeau, D. A. Unveiling Carbon Dioxide and Ethanol Diffusion in Carbonated Water-Ethanol Mixtures

- by Molecular Dynamics Simulations. *Molecules* **2021**, *26* (6), 1711. https://doi.org/10.3390/molecules26061711.
- (67) Bahreini, R.; Keywood, M. D.; Ng, N. L.; Varutbangkul, V.; Gao, S.; Flagan, R. C.; Seinfeld, J. H.; Worsnop, D. R.; Jimenez, J. L. Measurements of Secondary Organic Aerosol from Oxidation of Cycloalkenes, Terpenes, and m -Xylene Using an Aerodyne Aerosol Mass Spectrometer. *Environ. Sci. Technol.* **2005**, *39* (15), 5674–5688. https://doi.org/10.1021/es048061a.
- (68) Ambrose, D.; Sprake, C. H. S.; Townsend, R. Thermodynamic Properties of Organic Oxygen Compounds XXXIII. The Vapour Pressure of Acetone. *J. Chem. Thermodyn.* **1974**, *6* (7), 693–700. https://doi.org/10.1016/0021-9614(74)90119-0.
- (69) Levelt Sengers, J. M. H.; Chen, W. T. Vapor Pressure, Critical Isochore, and Some Metastable States of CO 2. *J. Chem. Phys.* **1972**, *56* (1), 595–608. https://doi.org/10.1063/1.1676911.
- (70) Meyers, C. H.; Van Dusen, M. S. The Vapor Pressure of Liquid and Solid Carbon Dioxide. *Bur. Stand. J. Res.* **1933**, *10* (3), 381. https://doi.org/10.6028/jres.010.029.
- (71) Liang, Z.; Zhang, R.; Gen, M.; Chu, Y.; Chan, C. K. Nitrate Photolysis in Mixed Sucrose–Nitrate–Sulfate Particles at Different Relative Humidities. *J. Phys. Chem. A* **2021**, *125* (17), 3739–3747. https://doi.org/10.1021/acs.jpca.1c00669.
- (72) Pöschl, U.; Martin, S. T.; Sinha, B.; Chen, Q.; Gunthe, S. S.; Huffman, J. A.; Borrmann, S.; Farmer, D. K.; Garland, R. M.; Helas, G.; Jimenez, J. L.; King, S. M.; Manzi, A.; Mikhailov, E.; Pauliquevis, T.; Petters, M. D.; Prenni, A. J.; Roldin, P.; Rose, D.; Schneider, J.; Su, H.; Zorn, S. R.; Artaxo, P.; Andreae, M. O. Rainforest Aerosols as Biogenic Nuclei of Clouds and Precipitation in the Amazon. *Science* **2010**, *329* (5998), 1513–1516. https://doi.org/10.1126/science.1191056.

TOC Graphic



Supporting Information: Boiling of catechol secondary organic aerosol when heated to mild temperatures (36-52 °C) due to carbon dioxide formation and high viscosity

Kristian J. Kiland, ^{1,†} Katherine S. Hopstock, ² Ayomide A. Akande, ¹ Kristen N. Johnson, ² Yixin Li, ² Fabian Mahrt, ^{1,‡} Sepehr Nikkho, ¹ Barbara J. Finlayson-Pitts, ² Nadine Borduas-Dedekind, ¹ Sergey A. Nizkorodov, ² and Allan K. Bertram^{1,*}

- 1 Department of Chemistry, The University of British Columbia, Vancouver V6T 1Z1 British Columbia, Canada
- 2 Department of Chemistry, University of California, Irvine, Irvine, CA 92697, USA.
- † Now at the Department of Integrative Oncology, British Columbia Cancer Research Institute, Vancouver V5Z 1L3, British Columbia, Canada.
- ‡ Now at the Department of Chemistry, Aarhus University, Aarhus 8000, Denmark.

S1 Relevant chemical structures

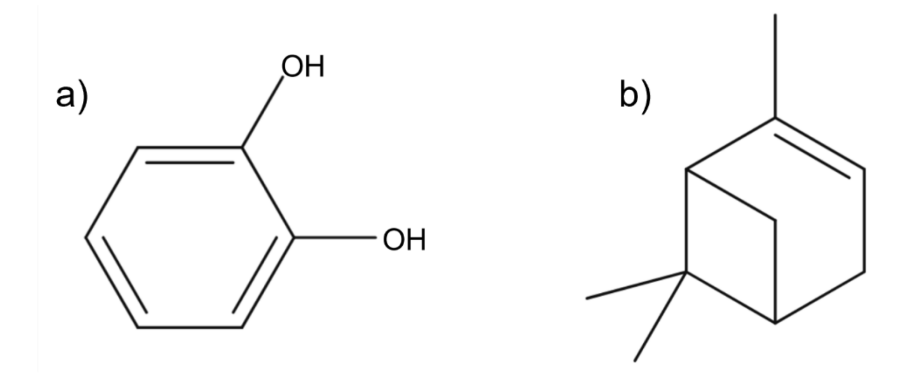


Figure S1. Chemical structures of (a) catechol and (b) α -pinene.

S2 Schematic of imaging experiments

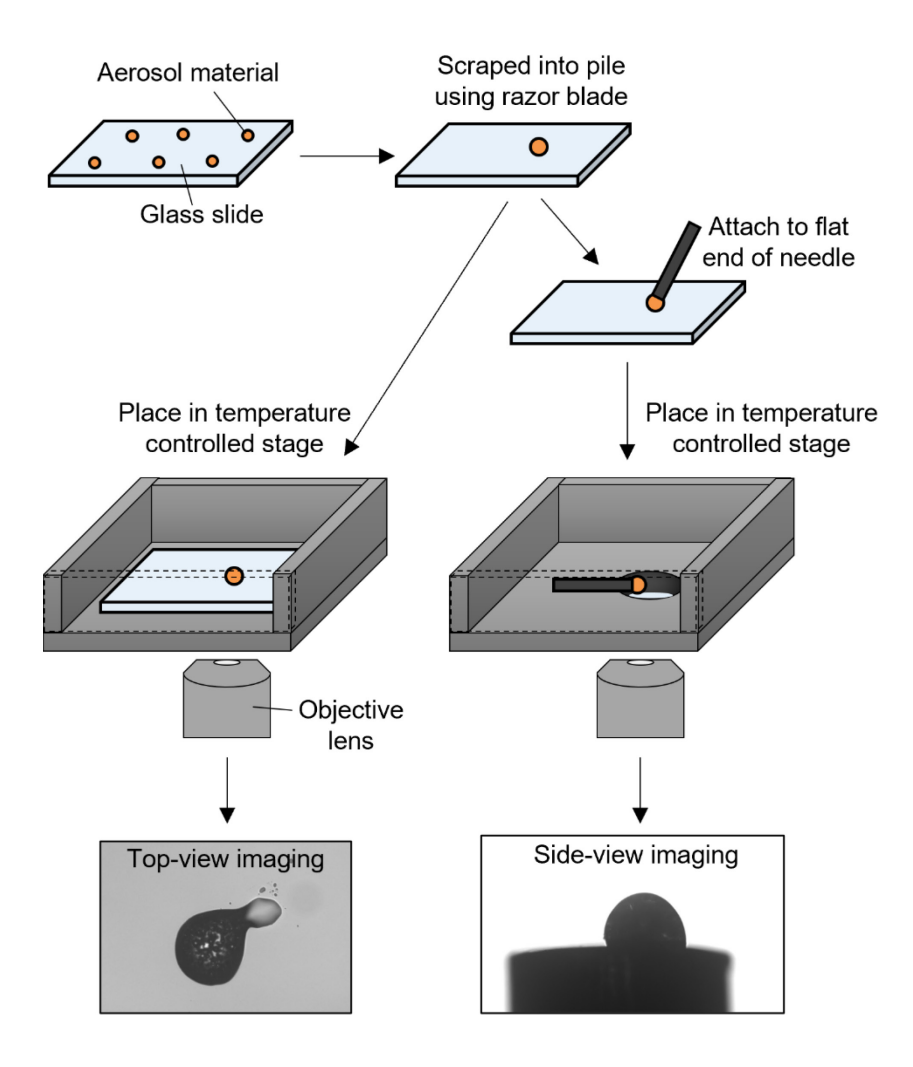


Figure S2. Schematic of the different types of sample preparation for particle imaging. Aerosol material was collected from the environmental chamber onto a glass slide using a multi-orifice single-stage impactor. The material was then scraped into a pile using a razor blade. For top-view imaging, the glass slide was directly placed into the temperature-controlled cell, which was mounted above a microscope. For side-view imaging, the material was attached to the flat end of a needle, which was then placed into the temperature-controlled cell.

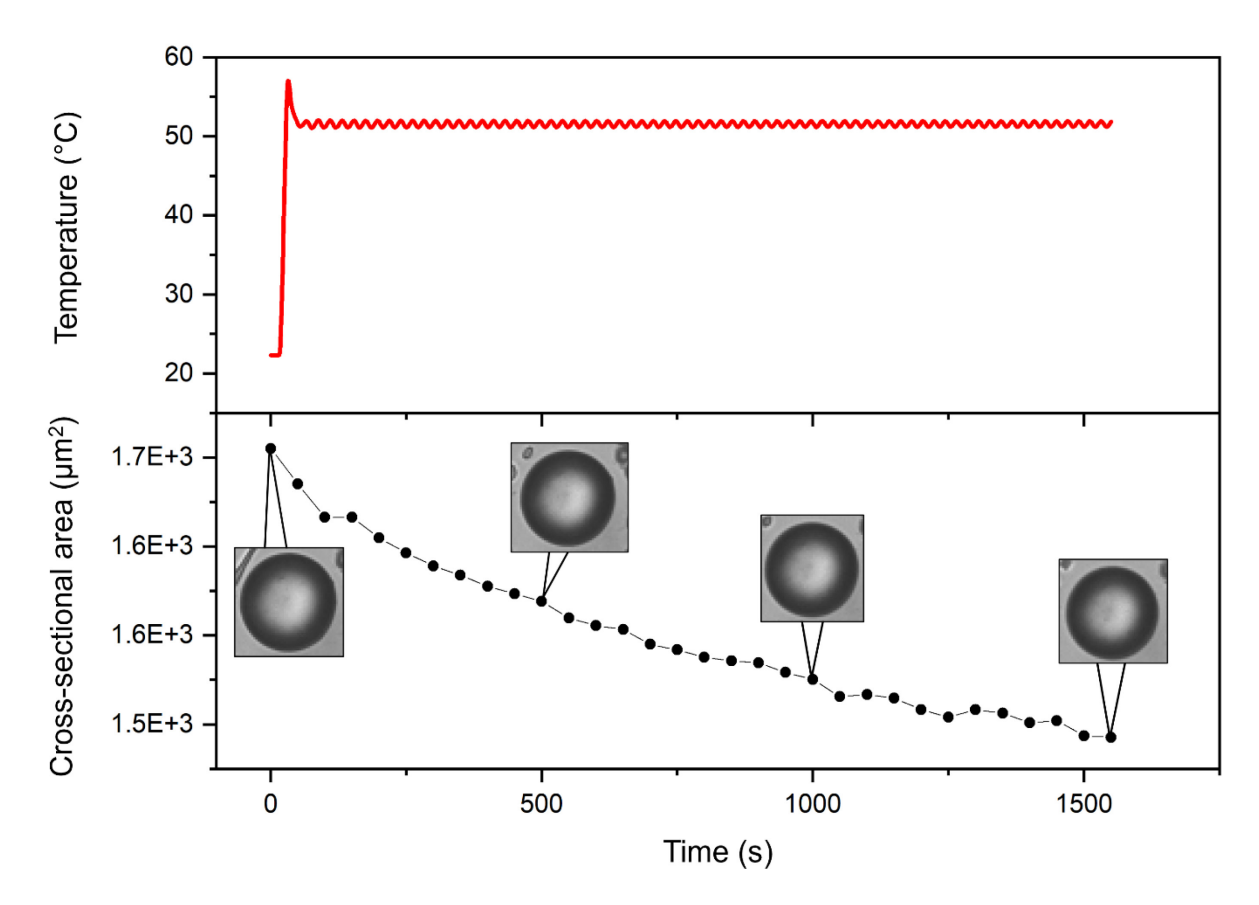


Figure S3. Imaging results from heating experiments with α-pinene SOA. The top panel shows the temperature profile during heating (T = 52 °C). Corresponding cross-sectional areas of the α-pinene SOA particle (bottom panel) are shown. Top-view images of the particle on a hydrophobic glass slide are provided alongside the data. During heating, the cross-sectional area decreased by ~10%. The particle shown here has a diameter of ~50 μm. Note, α-pinene SOA was too liquid-like (i.e., low viscosity) to scrape into a pile using a razor blade.

S3 PTR-MS flow cell background and correlation of C₃H₇O and C₃H₉O₂⁺

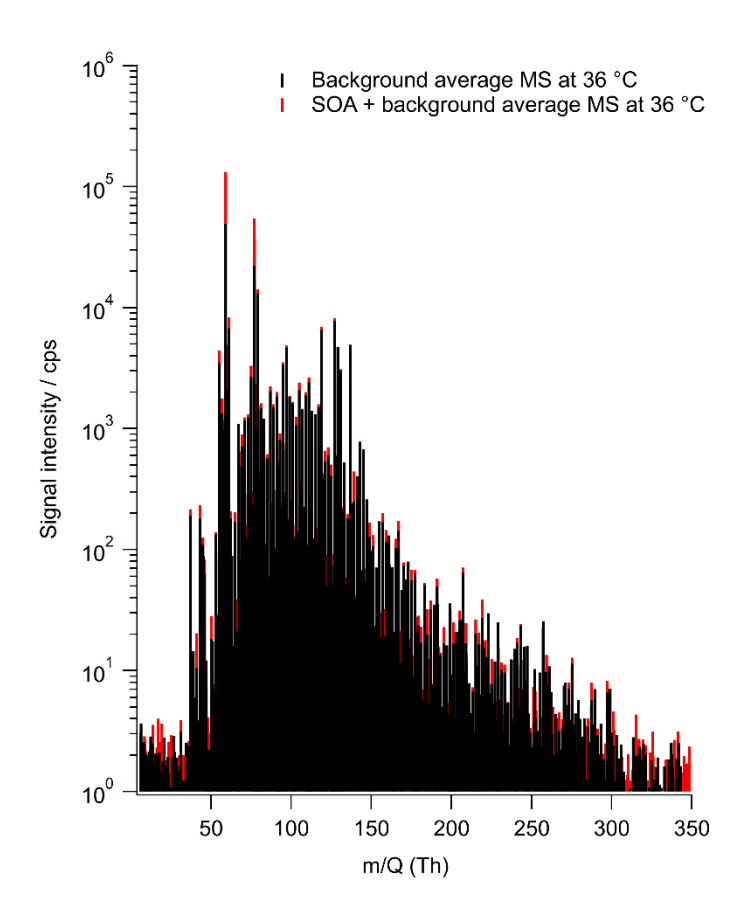


Figure S4. PTR-MS results for SOA samples heated to 36 °C. For clarity, only peaks up to m/Q 350 are shown, as peaks outside of the range were very small in comparison.

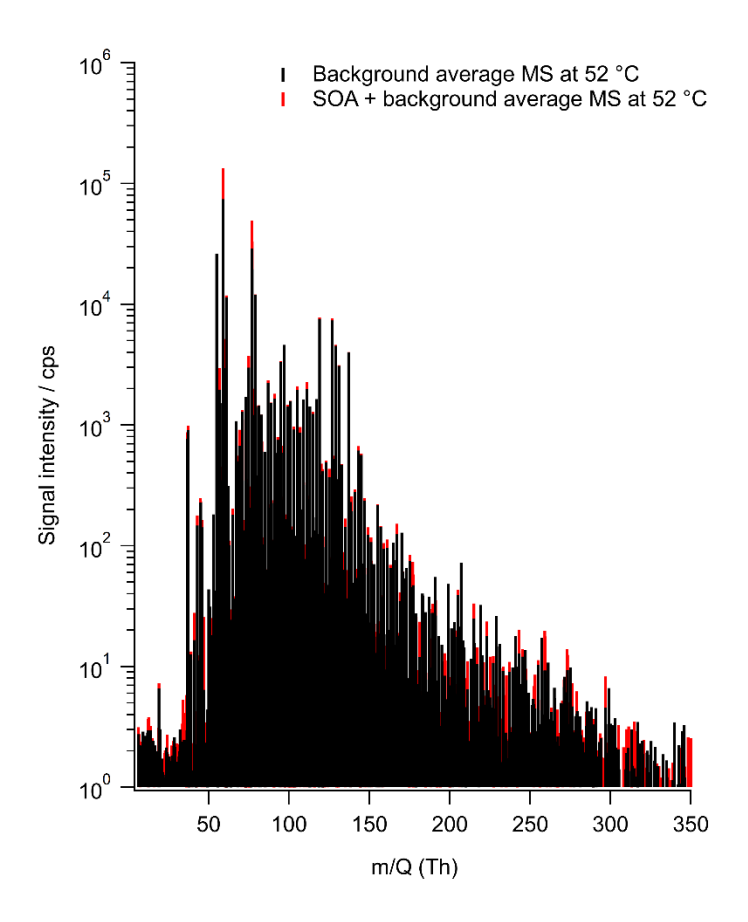


Figure S5. PTR-MS results for SOA samples heated to 52 °C. For clarity, only peaks up to m/Q 350 are shown, as peaks outside of the range were very small in comparison.

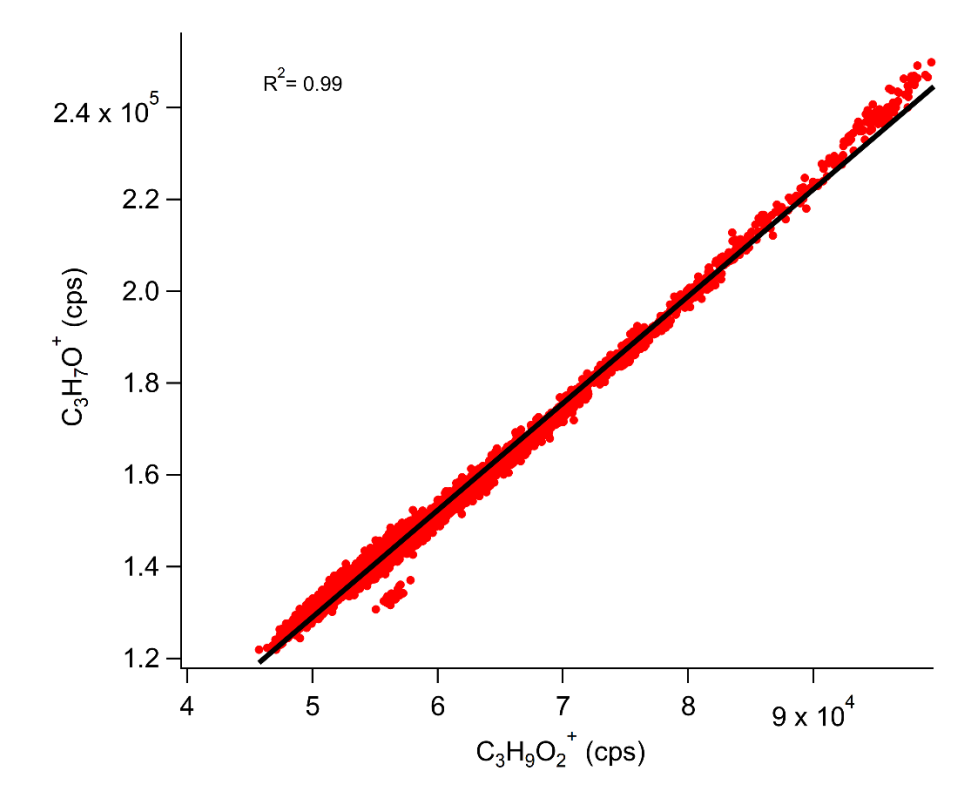


Figure S6. Scatter plot of $C_3H_7O^+$, likely acetone, and $C_3H_9O_2^+$, likely acetone-water cluster. The correlation plot has an R^2 of 0.99 suggesting that the two signals are strongly correlated in source.

S4 Detection of CO₂ from heated catechol SOA using EI-MS

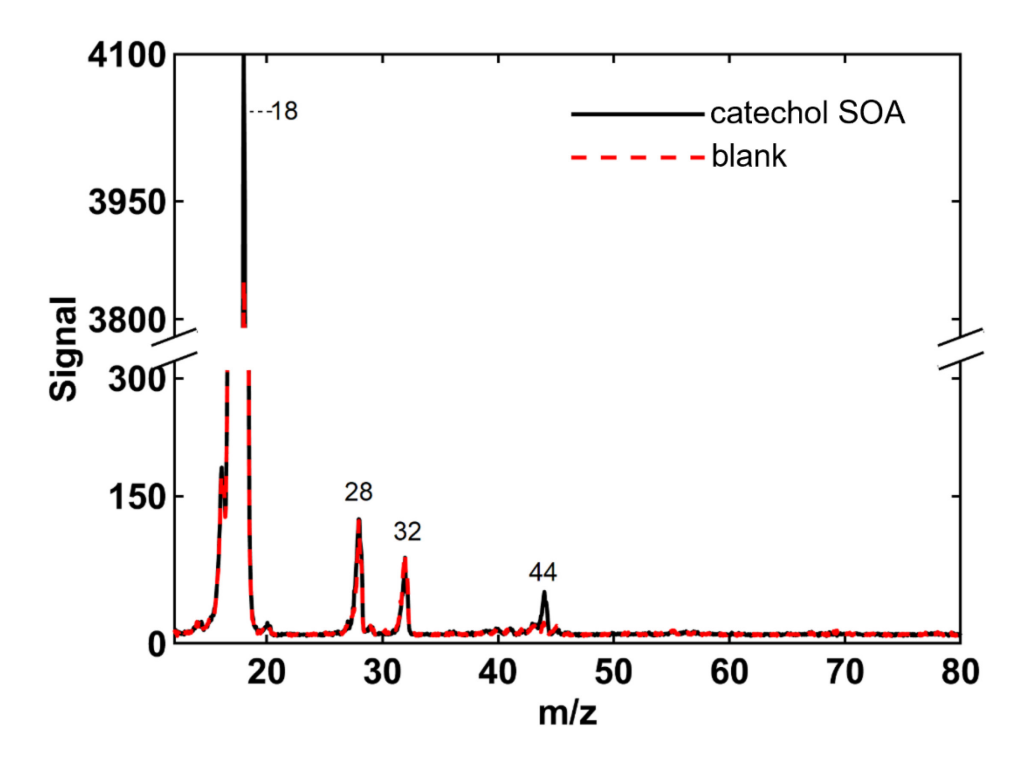


Figure S7. EI mass spectra collected from the heating of catechol SOA (solid black) and blank (dashed red) samples. The peaks at m/z 18, 28, 32, and 44 are assigned to water, nitrogen, oxygen, and carbon dioxide, respectively. The range m/z 80-250 is omitted because no peaks were identified.

S5 UHPLC-HESI-HRMS data summary and possible contamination

The most intense peaks from the UHPLC-HESI-HRMS experiments are summarized in Table S1. Two relatively large peaks in the unheated samples were at m/z 171.0663 (corresponding to neutral formula $C_8H_{12}O_4$) and 185.0820 (corresponding to neutral formula $C_9H_{14}O_4$). These peaks were assigned to terpenylic acid and pinic acid, respectively, which are α -pinene ozonolysis oxidation products and likely due to cross-contamination from α -pinene SOA generated in the same environmental chamber prior to generating catechol SOA. These peaks increased in relative intensity when the sample was heated to 52 °C, and we interpret this as a result of higher thermal stability of the α -pinene SOA compounds compared to the catechol SOA compounds (Fig. S8).

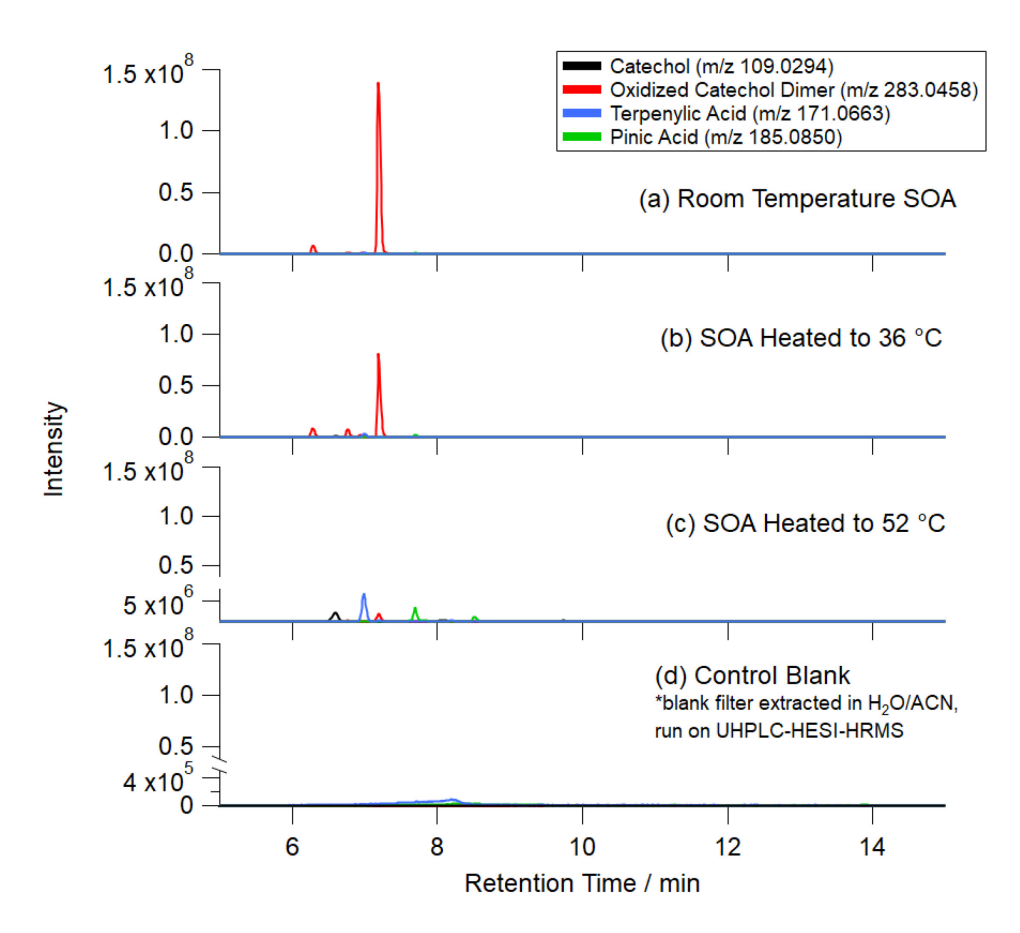


Figure S8. UHPLC-HESI-HRMS extracted ion chromatograms corresponding to catechol (black trace), oxidized catechol dimer (red trace), terpenylic acid (blue trace), and pinic acid (green trace) for room temperature SOA (a), SOA heated to 36 °C (b), SOA heated to 52 °C (c), and a control blank (d). The control blank represents a blank filter that was extracted in H₂O/ACN (1:1 *v/v*) and run on UHPLC-HESI-HRMS during the same sequence as the SOA samples. Terpenylic acid and pinic acid (monoterpene oxidation products) contamination peaks were not present in the control blank, but are present in the catechol ozonolysis SOA samples due to carryover from previous chamber experiments. The split axis in panel (c) demonstrates the decline of the oxidized catechol dimer peak and the enhancement of the contamination peaks. Note the split axis in panel (d) was used to further illustrate the lack of presence of these contamination species in the control blank.

For the samples heated to 52 °C, the mass spectra also showed many $C_{15}H_{24}O_x$ compounds, which can be assigned to sesquiterpene oxidation products. These compounds could theoretically be forming from catechol SOA degradation reactions, but more likely the collected SOA was also contaminated with sesquiterpene products. Sesquiterpene SOA was also generated in the same environmental chamber prior to generating catechol SOA.

Table S1. Summary of the most intense peaks from the mass spectra in Figure 1. Peaks that are repeated amongst catechol SOA at different temperatures are presented in bold font.

Catechol + O ₃	Major	Major	Chemical	Percent	Possible assignments
SOA	observed	calculated	formula of	Normalized	
	m/z	m/z	neutral	Intensity (%)	
			species		
Room	109.0294	109.0295	C ₆ H ₆ O ₂	6	Catechol
Temperature	135.0451	135.0452	$C_8H_8O_2$	4	
	141.0193	141.0193	$C_6H_6O_4$	9	
	151.0764	151.0765	$C_9H_{12}O_2$	10	
	171.0663	171.0663	$C_8H_{12}O_4$	15	Terpenylic acid*
	177.0556	177.0557	$C_{10}H_{10}O_3$	14	
	185.0820	185.0819	$C_9H_{14}O_4$	10	Pinic acid*
	195.0663	195.0663	$C_{10}H_{12}O_4$	8	
	221.0454	221.0455	$C_{11}H_{10}O_5$	26	
	239.0561	239.0561	$C_{11}H_{12}O_6$	10	
	283.0458	283.0459	$C_{12}H_{12}O_8$	100	Oxidized catechol dimer
	305.0278	-	-	5	
	382.9711	-	-	5	
Heated	109.0294	109.0295	$C_6H_6O_2$	5	Catechol
36 °C	141.0193	141.0193	$C_6H_6O_4$	13	
	151.0764	151.0765	$C_9H_{12}O_2$	10	
	171.0663	171.0663	$C_8H_{12}O_4$	13	Terpenylic acid*
	177.0557	177.0557	$C_{10}H_{10}O_3$	18	
	179.0351	179.0350	$C_9H_8O_4$	5	
	185.0820	185.0819	$C_9H_{14}O_4$	13	Pinic acid*
	195.0662	195.0663	$C_{10}H_{12}O_4$	8	
	221.0454	221.0455	$C_{11}H_{10}O_5$	31	
	239.0561	239.0561	$C_{11}H_{12}O_6$	10	
	283.0457	283.0459	$C_{12}H_{12}O_8$	100	Oxidized catechol dimer
	299.0408	299.0409	$C_{12}H_{12}O_9$	14	
	305.0275	-	-	7	
	319.0826	319.0823	$C_{16}H_{16}O_{7}$	6	
	355.1035	355.1035	$C_{16}H_{20}O_{9}$	4	
Heated	109.0294	109.0295	$C_6H_6O_2$	19	Catechol
52 °C	171.0663	171.0663	$C_8H_{12}O_4$	51	Terpenylic acid*
	185.0820	185.0819	$C_9H_{14}O_4$	38	Pinic acid*
	251.1653	251.1653	$C_{15}H_{24}O_3$	57	_*
	253.1447	253.1445	$C_{14}H_{22}O_4$	47	
	267.1603	267.1602	$C_{15}H_{24}O_4$	42	_*
	283.1551	283.1551	$C_{15}H_{24}O_5$	16	
	293.1759	293.1758	$C_{17}H_{26}O_4$	100	
	297.1531	-	-	38	
	299.1499	299.1500	$C_{15}H_{24}O_6$	40	_*

^{*} Possible sesquiterpene contamination.

S6 Supplemental Video Descriptions

Video S1. Imaging of catechol SOA during a temperature ramp experiment (corresponding to Fig. 1 in the main text). The particle was attached to a needle to capture side-view images. The initial area-equivalent diameter of the particle (at t=0) was 132 μ m, which grew to a maximum of 259 μ m at 1725 s. Note that the temperature values in the video haven't been corrected for the offset of the temperature-controlled cell, so the actual temperatures are ~0–5 °C higher than shown here. The correct temperatures are shown in Fig. 1

Video S2. Imaging of catechol SOA during heating to 36 °C (corresponding to Fig. 2 in the main text). The particle was attached to a needle to capture side-view images. The initial area-equivalent diameter of the particle (at t=0) was ~150 µm. Note that the temperature values in the video haven't been corrected for the offset of the temperature-controlled cell, so the actual temperatures are ~1 °C higher than shown here. The correct temperatures are shown in Fig. 2.

Video S3. Imaging of catechol SOA during heating to 52 °C (corresponding to Fig. 3 in the main text). The particle was placed on a hydrophobic glass slide to capture top-view images. The initial area-equivalent diameter of the particle (at t=0) was ~150 µm. Note that the temperatures in the video haven't been corrected for the offset of the temperature-controlled cell, so the actual temperatures are ~2 °C higher than shown here. The correct temperatures are shown in Fig. 3.

References

Zhao, Z., Yang, X., Lee, J., Tolentino, R., Mayorga, R., Zhang, W. and Zhang, H.: Diverse Reactions in Highly Functionalized Organic Aerosols during Thermal Desorption, ACS Earth Sp. Chem., 4(2), 283–296, doi:10.1021/acsearthspacechem.9b00312, 2020.